EUROPEAN ORGANIZATION FOR NUCLEAR RESEARCH (CERN)

CERN-EP-2025-168
LHCb-PAPER-2025-024
November 13, 2025

arXiv:2508.20180v2 [hep-ex] 14 Nov 2025

Inclusive B-meson flavour-tagging algorithm at LHCb

LHCb collaboration[†]

Abstract

A new algorithm is developed to identify the flavour of neutral B mesons at production in pp collisions by utilising all tracks from the hadronisation process. The algorithm is calibrated separately for B^0 and B_s^0 mesons using $B^0 \to J/\psi K^+\pi^-$ and $B_s^0 \to D_s^-\pi^+$ decays from pp collision data collected by the LHCb experiment at a centre-of-mass energy of 13 TeV. This new algorithm improves the tagging power by 35% for B^0 mesons and 20% for B_s^0 mesons when compared to the combined performance of the existing LHCb flavour-tagging algorithms.

Published in JHEP 11 (2025) 041

© 2025 CERN for the benefit of the LHCb collaboration. CC BY 4.0 licence.

[†]Authors are listed at the end of this paper.

1 Introduction

Measurements of flavour oscillation frequencies [1,2] and time-dependent charge-parity (CP) asymmetries of neutral B mesons [3,4] require knowledge of the signal B-meson flavour at production. The experimental technique to determine this information at collider experiments is referred to as flavour tagging.

At the LHCb experiment, dedicated algorithms are used to infer the production flavour by exploiting the production and decay mechanisms of B mesons in pp collisions. They are classified into two types of algorithms, opposite-side (OS) and same-side (SS) taggers. The OS taggers [5,6] exploit the fact that b quarks are predominantly produced in $b\bar{b}$ pairs, and thus the flavour at production of the reconstructed B meson is opposite to that of the other b hadron in the event, referred to as the opposite-side b hadron. Therefore, flavour tagging can be performed using the decay products of the accompanying b hadron in the event. The five OS taggers in use at LHCb are based on muons, electrons, kaons, charm decays and the charge of the B decay vertex. The SS taggers [7,8] use charged particles produced in the hadronisation process in association with the reconstructed signal B meson. For B_s^0 mesons, the SS tagger uses a charged kaon and for B^0 mesons, a charged pion or a proton. The charge of these particles indicates the b-quark content of the B meson. Information from SS and OS algorithms is usually combined in flavour-tagged analyses to increase the measurement precision. Flavour-tagging algorithms provide an event-by-event tagging decision as well as a mistag estimation η that gives the probability of a false decision, which needs to be calibrated on control samples of flavour-specific decays to determine the mistag probability $\omega(\eta)$ of the event.

The performance of a flavour-tagging algorithm is measured by its tagging power ε_{eff}, which is defined as

$$\varepsilon_{\text{eff}} = \varepsilon_{\text{tag}}\langle D^2\rangle, \qquad D = 1 - 2\omega, \tag{1}$$

where ε_{tag} denotes the fraction of events that have a tagging decision and D is the per-event dilution. Mistagged candidates reduce the oscillation amplitudes and therefore the statistical power of flavour-tagged data. Notably, the dilution factor $\langle D^2\rangle$ is obtained by averaging D^2 over all events. The tagging power quantifies the effective statistical sample size, making improved flavour tagging essential to maximise the precision of the oscillation-related observables. In the case of weighted events ε_{tag} and $\langle D^2\rangle$ are computed as

$$\varepsilon_{\text{tag}} = \frac{\sum_j w_j}{\sum_i w_i}, \qquad \langle D^2\rangle = \frac{\sum_j w_j(1-2\omega_j)^2}{\sum_j w_j}, \tag{2}$$

where w is the per-event weight and the index i runs over all events, while the index j runs over the subset of tagged events.

This paper describes a new approach called *inclusive flavour tagging* (IFT), which exploits the available information in a pp collision event containing a $b\bar{b}$ pair at a more global level than the SS and OS taggers [9]. Instead of searching for information that matches particular underlying physics processes as the SS and OS tagging algorithms do, the IFT includes information from the majority of charged-particle tracks produced in an event. A similar technique, developed for electron-positron collisions, was recently implemented at the Belle II experiment [10] and showed improvement over existing methods.

The IFT presented here is based on a deep neural network architecture DeepSets [11]. Two IFT algorithms, one for B^0 mesons and one for B_s^0 mesons, are trained on simulated $B^0 \to J/\psi[\to \mu^+\mu^-]K^*(892)^0\,[\to K^+\pi^-]$ and $B_s^0 \to J/\psi[\to \mu^+\mu^-]\phi(1020)\,[\to K^+K^-]$ decays, respectively.[1,2] Each algorithm returns an independent event-by-event probability $y \in [0,1]$, from which a tagging decision d and a mistag prediction η are set according to the value of y as

$$d = \begin{cases} +1 & \text{if} \quad y > 0.5\,, \\ 0 & \text{if} \quad y = 0.5\,, \\ -1 & \text{if} \quad y < 0.5\,, \end{cases} \tag{3}$$

where $+1$ corresponds to a B meson and -1 to $\overline{B}$ meson, and

$$\eta = \begin{cases} 1 - y & \text{if} \quad y > 0.5\,, \\ y & \text{if} \quad y \leq 0.5\,. \end{cases} \tag{4}$$

The mistag probabilities are calibrated on $B^0 \to J/\psi K^+\pi^-$ decays, where the kaon-pion pair lies within the mass range of the $K^*(892)^0$ resonance, and on $B_s^0 \to D_s^-\pi^+$ decays using pp collision data collected by the LHCb experiment at a centre-of-mass energy of 13 TeV during Run 2. This calibration is essential because the classifiers are trained on simulated samples, which do not perfectly replicate the characteristics of LHCb data. The IFT is validated on $B^0 \to J/\psi K_S^0\,[\to \pi^+\pi^-]$ decays and $B_s^0 \to J/\psi K^+K^-$ decays in the vicinity of the ϕ resonance.

All studies are performed independently on the samples collected in the years 2016, 2017 and 2018 to account for possible differences between the data collected in varying data-taking conditions.

2 Detector and simulation

The LHCb detector [12, 13] is a single-arm forward spectrometer covering the pseudorapidity range between 2 and 5, designed for the study of particles containing b or c quarks. The detector used for these studies includes a high-precision tracking system consisting of a silicon-strip vertex detector (VELO) surrounding the pp interaction region [14], a large-area silicon-strip detector (TT) located upstream of a dipole magnet with a bending power of about 4 T m, and three stations of silicon-strip detectors and straw drift tubes [15] placed downstream of the magnet. The tracking system provides a measurement of the momentum, p, of charged particles with a relative uncertainty that varies from 0.5% at low momentum to 1.0% at 200 GeV/c. The minimum distance of a track to a primary pp collision vertex (PV), the impact parameter (IP), is measured with a resolution of $(15 + 29/p_{\mathrm{T}})\,\mu$m, where p_{T} is the component of the momentum transverse to the beam, in GeV/c. Different types of charged hadrons are distinguished using information from two ring-imaging Cherenkov detectors [16]. Photons, electrons and hadrons are identified by a calorimeter system consisting of scintillating-pad and preshower detectors, an electromagnetic and a hadronic calorimeter. Muons are identified by a system composed of alternating layers of iron and multiwire proportional chambers [17].

[1]The inclusion of charge-conjugate processes is implied throughout this paper, unless otherwise noted.
[2]For simplicity, the resonances $K^*(892)^0$ and $\phi(1020)$ are referred to as K^{*0} and ϕ in the following.

The online event selection is performed by a trigger [18], which consists of a hardware stage, based on information from the calorimeter and muon systems, followed by a software stage, which applies a full event reconstruction. At the hardware trigger stage, events are required to have a muon with high p_{T} or a hadron, photon or electron with high transverse energy in the calorimeters. Following the hardware trigger stage, different software trigger algorithms are applied depending on the decay mode, following the strategy of Refs. [2–4].

In the modes containing a J/ψ meson, the trigger relies on reconstructing the $J/\psi \to \mu^+\mu^-$ decay and identifying candidates consistent with a J/ψ meson displaced from the PV associated with the signal B-meson decay. In the $B_s^0 \to D_s^-\pi^+$ decay mode, the first-stage software trigger applies a multivariate algorithm to select either a good-quality track with a high p_{T} or a good-quality two-track secondary vertex. In the second stage, the software trigger selects candidates consistent with a b-hadron decay topology, with a two-, three-, or four-track vertex with a sizeable p_{T} and a significant displacement from any PV. Note that the hadron trigger applies stricter p_{T} requirements than the dimuon trigger, leading to a p_{T} spectrum that is shifted toward higher values.

Simulated events are used to train the flavour-tagging algorithms, to model the signal mass and the decay-time distributions, to verify the analysis procedure and to study systematic effects. In the simulation, pp collisions are generated using Pythia [19] with a specific LHCb configuration [20]. Decays of unstable particles are described by EvtGen [21], in which final-state radiation is generated using Photos [22]. The interaction of the generated particles with the detector, and its response, are implemented using the Geant4 toolkit [23] as described in Ref. [24].

3 Inclusive flavour-tagger training

In pp collision events, the tracks observed after excluding those associated with the signal B-meson decay can be grouped into four categories. The first category includes light charged hadrons, such as pions, kaons or protons, produced during the hadronisation process along with the signal B meson. It is referred to as a same-side-fragmentation (SSF) track category and is used by the SS taggers. The second category includes tracks associated with the decay of an opposite-side b hadron, referred to as opposite-side-decay (OSD) tracks. These OSD tracks are the types of tracks used by the OS algorithms. Another category consists of light charged hadrons produced in the fragmentation of the opposite-side b hadron that are referred to as opposite-side-fragmentation (OSF) tracks. The last category consists of the remaining tracks originating from the pp collision, referred to as underlying tracks. These are considered background for the purposes of flavour tagging.

All four track categories are included in the IFT. The SSF, OSD and OSF categories carry information on the initial flavour of the signal B meson, in particular through the charge of the track and additional particle-identification (PID) information. The information provided by the OSD and OSF categories is nearly independent of the signal B-meson kinematics. On the other hand, the type of SSF track depends on the type of the light quark in the signal B meson. Pions and protons are produced along with a B^0 meson, while kaons are produced along with a B_s^0 meson. Therefore, to achieve an optimal performance, the classifiers for B^0 and B_s^0 mesons are trained independently on different samples. The B^0 tagger is trained on simulated events containing $B^0 \to J/\psi K^{*0}$ decays

and the B_s^0 tagger on simulated events containing $B_s^0 \to J/\psi\phi$ decays.

Another aspect to consider for the construction of the neural network is the variation of the number of tracks in each event. The data samples of this study were collected at an instantaneous luminosity of $2 \times 10^{33}\,\mathrm{cm}^{-2}\,\mathrm{s}^{-1}$, for which the number of reconstructed tracks per event is approximately 40, with a small fraction of events containing more than 100 tracks. The DeepSets neural network architecture allows a variable number of inputs, making it a suitable choice of classifier. In addition, it provides an advantage in training duration that is an order of magnitude shorter than similar architectures such as recurrent neural networks. DeepSets architectures have been successfully employed in the development of flavour-tagging methods, such as in the OS jet tagger by the CMS collaboration [25].

3.1 Training samples

The simulated $B^0 \to J/\psi K^{*0}$ and $B_s^0 \to J/\psi\phi$ samples used for training are generated under Run 2 detector and accelerator conditions. Events must satisfy trigger requirements and additional selection criteria, consistent with those applied to data. The signal B-meson candidate is reconstructed from its charged decay products, while the remaining tracks in each event are used as input for the tagger training.

The chosen simulated samples correspond to decay channels with B-meson candidates selected by loose trigger requirements, ensuring coverage of a broad kinematic region. For the B^0 tagger, simulated flavour-specific $B^0 \to J/\psi K^{*0}$ decays are used for training and the corresponding data sample, $B^0 \to J/\psi K^+\pi^-$, is used for mistag calibration. The charge of the final-state pion identifies the flavour at decay time, enabling calibration through a time-dependent analysis of the flavour-tagged decay rate. For the B_s^0 tagger, training is performed using the $B_s^0 \to J/\psi\phi$ simulated sample, while calibration of the mistag probability is done using a data sample of the flavour-specific $B_s^0 \to D_s^-\pi^+$ decay. This strategy is chosen because a tagger trained on $B_s^0 \to J/\psi\phi$ generalizes better to other B_s^0 decay modes, such as $B_s^0 \to D_s^-\pi^+$, than vice versa. This is primarily due to the broader kinematic range of $B_s^0 \to J/\psi\phi$ decays enabled by less stringent trigger requirements, see Sec. 2, which allows the classifier to learn across the full kinematic phase space.

3.2 The DeepSets classifier

The DeepSets [11] process flow is illustrated in Fig. 1. Unlike a standard feed-forward network, which takes a single fixed-length feature vector as input, DeepSets operates on a variable-sized set of vectors $\vec{x}_i$. Each input vector corresponds to a track and contains relevant features, which are described in the following sections. For convenience, these vectors are arranged in a matrix X. The matrix is passed through a feed-forward neural network, denoted ϕ, which maps each input vector, *i.e.* each matrix column, individually to a higher-level representation. The resulting set of transformed vectors is then aggregated through a permutation-invariant pooling operation (a simple summation). In this way, the overall output is insensitive to the ordering of the tracks, even though the ϕ network itself acts on individual tracks. Finally, the pooled representation is passed to a second feed-forward network, ρ, which produces the final network response, $S(X) = \rho(\sum_i \phi(\vec{x}_i))$. In the implementation used for the IFT, the ϕ network contains an input layer followed

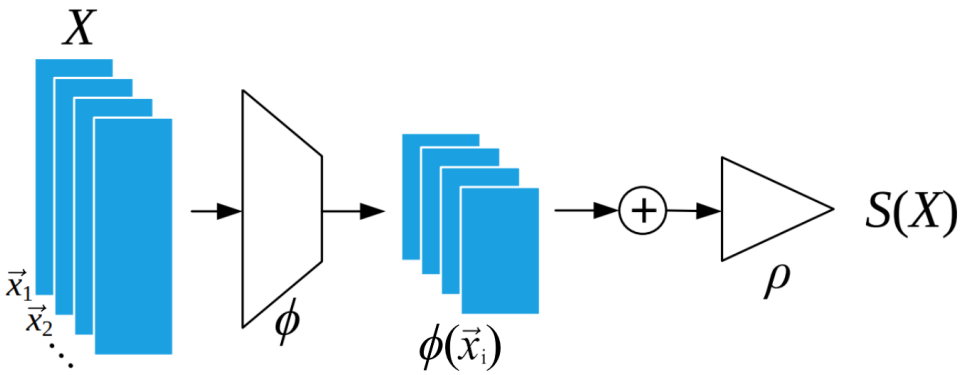

Figure 1: Illustrative representation of DeepSets: The neural network response S is inferred from the input matrix X based on two processing steps. First, a feed-forward neural network, ϕ, is applied to each feature vector $\vec{x_i}$ of the input matrix. The resulting sequence of output vectors $\phi(\vec{x_i})$ is then summed up into a single vector, which is evaluated by another feed-forward neural network, ρ. Figure adapted from Ref. [11].

by two hidden layers of equal size, while the ρ network consists of a hidden layer and an output layer with a single node.

The weights and biases of both networks are optimized during training. A rectified linear unit is used as the activation function in the hidden layers. The training is performed by minimizing the binary cross-entropy loss, evaluated over mini-batches and updated through backpropagation. A sigmoid activation ensures that the output of $S(X)$, the classification score y, is constrained to the interval $[0, 1]$. The value of y indicates whether the signal B meson contained a b quark ($y = 0$) or a $\bar{b}$ quark ($y = 1$) at production. In total, the network architecture contains 3890 trainable parameters.

3.3 Classifier training

The training of each tagger on its corresponding simulated sample proceeds in two steps. First, to reduce the complexity of the task faced by the DeepSets network, a multiclass boosted decision tree (BDT) classifier is trained using the XGBoost toolkit [26–28]. The BDT classifier assigns each track a probability of belonging to one of four categories: SSF, OSD, OSF and underlying event tracks. These category probabilities serve as inputs for the second stage, where a DeepSets neural network is trained to distinguish between the two B-meson production flavours. The network's output is the final prediction score, denoted by y.

The tracks used for training are required to have hits in at least the VELO and the TT, and must additionally satisfy the following criteria: momentum between 2 and 200 GeV/c; ghost probability lower than 0.35; $\arctan(p_{\mathrm{T}}/p_z) > 0.012$, where p_z refers to the momentum component parallel to the beam axis, which ensures that the track exhibits a sufficient angular separation from the beam axis. Both the BDT and the DeepSets classifiers use a common set of 23 track-related input features. The feature selection builds on the set originally proposed in the paper introducing the IFT algorithm [9]. The features include:

- PID information on whether the track is an electron, a muon, a pion, a kaon or a

proton; the probability that the track does not correspond to the genuine particle trajectory, referred to as ghost probability;

- track charge; p and p_{T} of the track; component of the track momentum along the signal B-meson momentum direction; ionisation charge deposited in the silicon layers of the VELO by the track;
- IP of the track with respect to the decay vertex of the signal B-meson candidate; IP of a track with respect to the PV associated to the signal B meson and the difference in χ^2 of a given PV reconstructed with and without the considered track; track-fit χ^2;
- difference between the pseudorapidities of the track and the signal B meson; cosine of the angular difference in azimuth between the track and signal B-meson momentum directions; difference along the beam line direction between the track origin and the PV associated to the signal B meson;
- BDT-based variable that uses all underlying tracks in the event to determine the isolation of the track.

The DeepSets network, in addition, includes the four output probabilities of the track-classification BDT per track, as well as information from the five OS and three SS taggers, mentioned in Sec. 1. For each of these, the corresponding mistag probability and tagging decision are combined into a single input variable $d(1-2\eta)$. The addition of the SS and OS taggers leads to a relative improvement in tagging power of approximately 5%. Note that even without them, the IFT performance exceeds that of the combined SS and OS taggers.

Since the training set includes a substantial fraction of tracks with limited information about the B-meson production flavour, *e.g.* tracks originating from different pp collisions of the event, a study was carried out to reduce their impact. In events with multiple PVs, such tracks are likely to be classified as background by the BDT. To reduce their impact, a preselection based on the background-related BDT output was tested prior to applying the DeepSets classifier. While this preselection successfully removed about 20% of the tracks without degrading tagging performance, it did not yield a significant improvement in training time or overall performance. Therefore, for simplicity, all tracks are retained in the current implementation. Nevertheless, the study suggests potential avenues for reducing complexity in future developments, particularly relevant for the LHCb upgrades, where the number of PVs and associated tracks is expected to increase significantly.

After the training, the distributions of the classifier output for the B^0 and B_s^0 taggers are displayed in Fig. 2, showing a separation between the two B-meson flavours. In the same figure, the corresponding receiver operating characteristic (ROC) curves are shown. They display the rates of correctly tagged events (true positives) against those of mistagged events (false positives) and serve as an initial indicator of the performance of the classifier.

4 Calibration of the mistag probability

The mistag probability estimated by the IFT algorithms is calibrated using data samples of flavour-specific $B^0 \to J/\psi K^+\pi^-$ and $B_s^0 \to D_s^-\pi^+$ decays. An unbinned maximum-

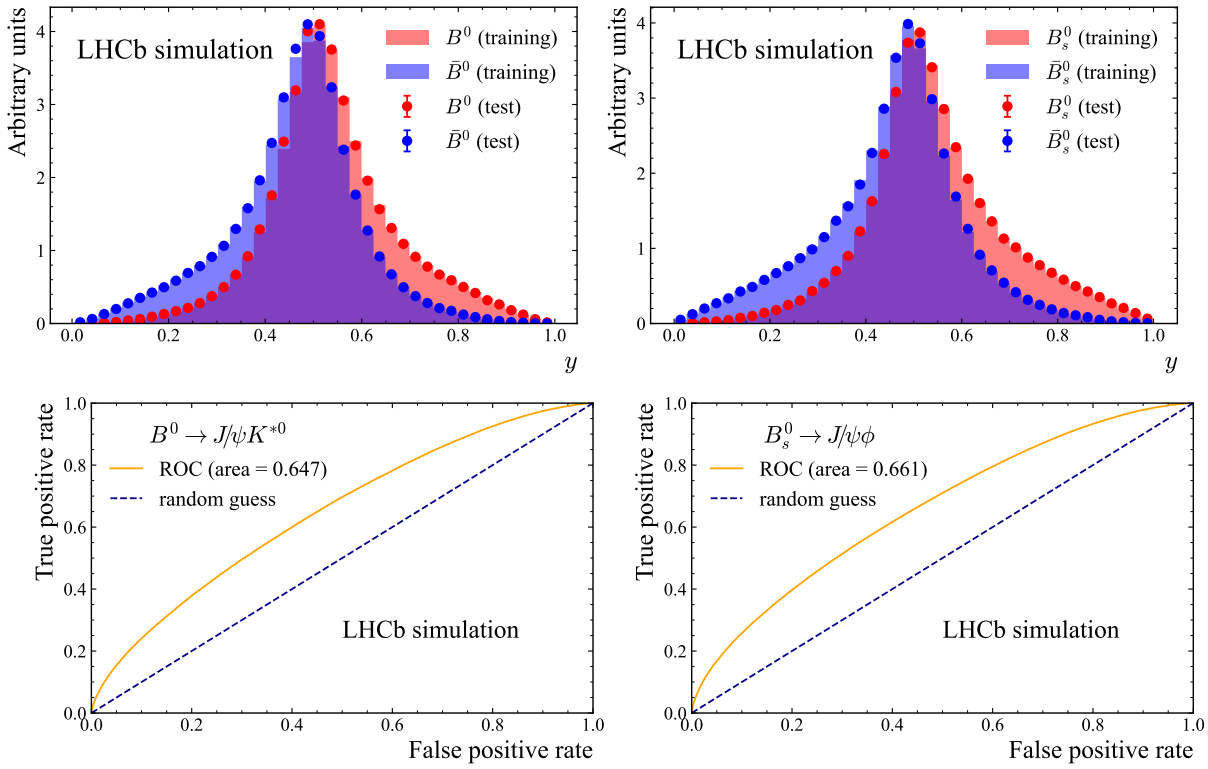

Figure 2: Distribution of the trained IFT classifier outputs y obtained from (top left) $B^0 \to J/\psi K^{*0}$ and (top right) $B_s^0 \to J/\psi\phi$ simulation, showing the training subsets and the test subsets and ROC curve compared to a random guess function of the trained (bottom left) $B^0 \to J/\psi K^{*0}$ and (bottom right) $B_s^0 \to J/\psi\phi$ simulated samples.

likelihood fit to the decay-time t is performed to resolve the neutral B-$\overline{B}$ flavour oscillation. The event-by-event decay-time resolution σ_t, estimated from a calibration of the decay-time uncertainty, is included as a conditional observable in the probability density function (PDF) $P(t|\sigma_t)$. A precise understanding of the decay-time resolution is crucial, especially for B_s^0 mesons, since a miscalibration can introduce a dilution of the oscillation amplitude that can be attributed to the flavour tagging. The PDF is a convolution of the neutral B-meson time-dependent decay rate $\Gamma(t)$ and the decay-time resolution function $G(t|\sigma_t)$, multiplied by the decay-time acceptance function $\epsilon(t)$,

$$P(t|\sigma_t) \propto \epsilon(t)\left[\Gamma(t') * G(t-t'|\sigma_t)\right]. \tag{5}$$

The decay-time acceptance for both calibration channels is modelled by cubic splines, whose parameters are allowed to vary in the fit. The decay-time resolution is modelled by a single Gaussian function, where σ_t is a per-candidate conditional variable. The neutral-B-meson time-dependent decay rate,

$$\Gamma(t|\eta, C_{\text{phys}}) \propto e^{-\Gamma_{d,s}t}\left[(1 - C_{\text{phys}}\Delta\omega(\eta))\cosh\left(\frac{1}{2}\Delta\Gamma_{d,s}t\right) + C_{\text{phys}}\left(1 - 2\omega(\eta)\right)\cos\left(\Delta m_{d,s}t\right)\right], \tag{6}$$

is a function of the difference between the heavy and light decay widths, $\Delta\Gamma_{d,s}$, and mass differences $\Delta m_{d,s}$, where the subscript d denotes B^0 mesons and s denotes B_s^0 mesons. The value of C_{phys} is $+1$ if the B-meson flavour at decay, identified by the charge of the

final-state pion, matches its flavour at the time of production, determined from the tagging decision. If the flavours do not match, C_{phys} is set to -1, and if the candidate is untagged it is set to 0. The parameters $\Delta\Gamma_s$, $\Delta m_{d,s}$, and $\Gamma_{d,s}$ are constrained to their known values by applying Gaussian penalty terms based on their respective uncertainties [4,29,30]. The value of $\Delta\Gamma_d$ is fixed to zero. The calibrated mistag probability ω is parametrised as a linear function of the estimated probability η,

$$\begin{aligned} \omega^{B}(\eta) &= p_0 + \frac{1}{2}\Delta p_0 + \left(p_1 + \frac{1}{2}\Delta p_1\right)(\eta - \bar{\eta}), \\ \omega^{\bar{B}}(\eta) &= p_0 - \frac{1}{2}\Delta p_0 + \left(p_1 - \frac{1}{2}\Delta p_1\right)(\eta - \bar{\eta}), \end{aligned} \tag{7}$$

where p_0 and p_1 are the linear function offset and slope, and $\bar{\eta}$ is the average estimated mistag probability of the sample. The factor $\Delta\omega(\eta) = \Delta p_0 + \Delta p_1(\eta - \bar{\eta})$ accounts for different mistag probabilities between B and $\overline{B}$ mesons. A second-order polynomial fit yields coefficients consistent with those of a linear model and therefore, the simpler functional form is adopted. Events in which the calibrated mistag probability exceeds 0.5 are treated as untagged. This results in a calibrated tagging efficiency lower than 100% for the IFT.

The ideal calibration value $p_1 = 1$ corresponds to the case where the predicted mistag η equals the calibrated mistag probability ω and the linear calibration model is exact. The values $\Delta p_{0,1} = 0$ indicate that there is no difference between the tagging of B mesons and $\overline{B}$ mesons. In practice, deviations from the ideal case arise from differences between data and simulation, residual model bias, detection asymmetries, model nonlinearity and species-dependent effects. This is what causes that ω differs from η, which is obtained from training on simulation. The calibration on data aims at correcting such discrepancies by matching ω to the observed mistag fraction in the data. Such effects have been observed in tagging algorithms both within and beyond LHCb (see e.g. Refs. [7,8,10]).

4.1 Calibration of the B^0 classifier

To reduce background contributions, loose requirements are applied on $B^0 \to J/\psi K^+\pi^-$ candidates, based on Ref. [4]. These include p_{T} and PID selections, which reduce backgrounds caused by misidentifying the pion as either a kaon or a proton.

The dominant remaining background is combinatorial, with a minor contribution from $B_s^0 \to J/\psi K^+\pi^-$ decays. These background contributions are subtracted using the *sPlot* [31] technique, based on an unbinned maximum-likelihood fit to the invariant mass of the B-meson candidates.

The mass distribution and corresponding fit result for the data sample combined over all data-taking years and C_{phys} values are shown in Fig. 3. The signal mass distribution is modelled with a Hypatia function [32] where the tail parameters are fixed from simulation, while the mean and width of the Gaussian core are free in the fit to the data. The same functional form is used to describe the $B_s^0 \to J/\psi K^+\pi^-$ contribution, differing only by a shift in the mean corresponding to the known $B_s^0 - B^0$ mass difference [29]. An exponential function is used to describe the combinatorial background contribution and its parameters are free in the fit to the data. The resulting signal yields are 399×10^3, 394×10^3 and 471×10^3 for 2016, 2017 and 2018, respectively.

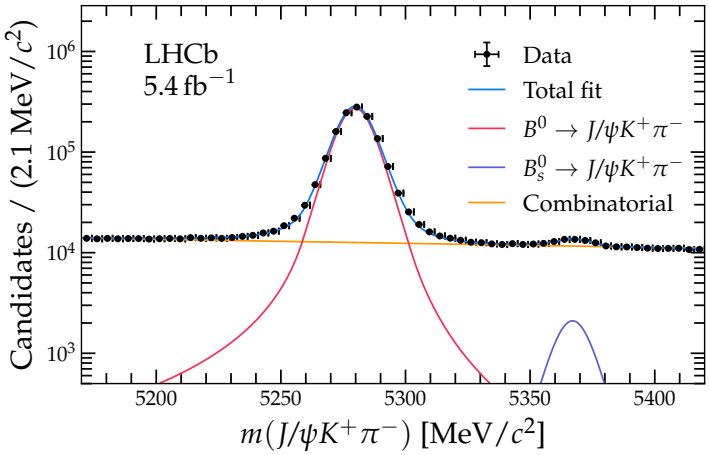

Figure 3: Invariant-mass distribution of $B^0 \to J/\psi K^+\pi^-$ candidates in the combined data sample with the result of the fit also shown.

The B^0 meson has an oscillation period that is significantly larger than the LHCb detector decay-time resolution. Therefore, for simplicity, the calibration of the decay-time resolution of $B^0 \to J/\psi K^+\pi^-$ decays is obtained from simulated decays instead of data. For this, the simulated dataset is split into eight bins of the reconstructed decay time. For each bin i an unbinned maximum-likelihood fit to the difference of the reconstructed and the true decay time is performed and is taken as the time resolution $\sigma_{t,i}$ of this bin. Subsequently, the effective decay-time resolution is obtained through a linear fit on $\sigma_{t,i}$ values. A linear dependence between the estimated and calibrated decay-time resolutions is assumed. To account for possible differences with the decay-time resolution in data, it is verified that variations of 5 times the statistical uncertainties on the calibration parameters do not affect the flavour-tagging performance. These variations also cover the case where no calibration is applied (*i.e.*, the calibrated decay-time resolution is identical to the uncalibrated one). This demonstrates that the decay-time resolution for B^0 decays has little influence on the tagging calibration.

A maximum-likelihood fit to the background-subtracted decay time of the $B^0 \to J/\psi K^+\pi^-$ sample is performed using Eq. 5 with inputs from Eq. 6. The fit result combined across all data-taking years and initial and final flavours is shown in Fig. 4. The resulting calibration function is shown in Fig. 5. The calibration parameters are summarised in Table 1. Their mutual correlations do not exceed 10%. Differences in the calibration parameters between data-taking years are small, yet significant enough to justify determining them independently.

4.2 Calibration of the B_s^0 classifier

The $B_s^0 \to D_s^-\pi^+$ candidates are selected through the $D_s^- \to K^+K^-\pi^-$ decay mode following the strategy of Ref. [2]. The purity of the sample is improved by imposing PID requirements on pions and kaons. Additional vetoes on the invariant masses of the D_s^- decay products are applied to suppress backgrounds from D^0 decays and from misidentified particles originating from D^- and Λ_c^- decays.

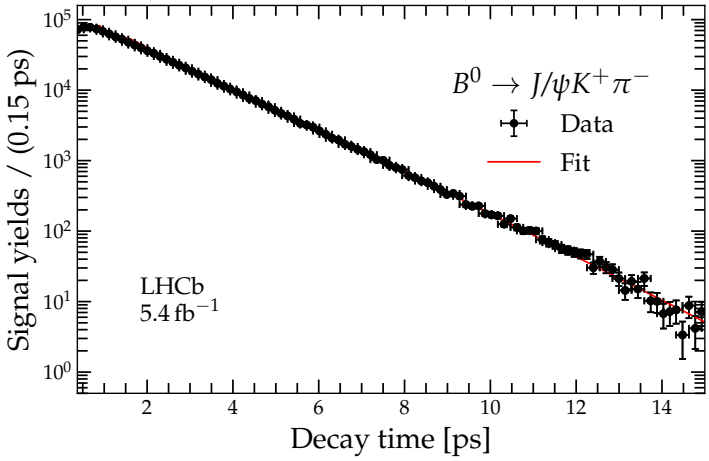

Figure 4: Background-subtracted decay-time distribution of $B^0 \to J/\psi K^+\pi^-$ candidates in the data sample combined across all data-taking years and initial and final flavours, together with the fit result.

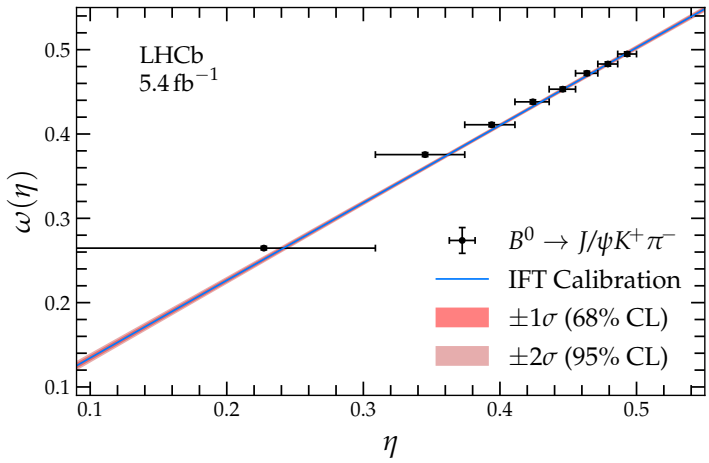

Figure 5: Measured mistag fraction ω as a function of the mistag probability η in $B^0 \to J/\psi K^+\pi^-$ data. The data points are obtained by performing a decay-time fit in each η bin and extracting the fraction of mistagged events.

As in the case of the B^0 classifier, the background in data is subtracted using the *sPlot* technique. The distribution of the B_s^0-meson candidate mass along with the fit to the data is shown in Fig. 6. Following the strategy of Ref. [4], the signal mass model is described by a Hypatia function and the combinatorial background is modelled with an exponential function. The background shapes of b-hadron decays, including $B_s^0 \to D_s^- K^+$, $B^0 \to D^-\pi^+$, $B_s^0 \to D_s^{*-}\pi^+$, $B_s^0 \to D_s^-\rho^+$ and $\Lambda_b^0 \to \Lambda_c^-\pi^+$, are modelled based on simulated samples. The background subtraction is performed in two steps. First, a fit to the invariant-mass distribution of the B_s^0 candidates in the region $[5100, 5600]\,\mathrm{MeV}/c^2$ is performed, in which the signal shape parameters are fixed to the values obtained from simulation. The shape parameter of the combinatorial background and the fractions of

Table 1: Results of the unbinned decay-time fit for the IFT calibration parameters in $B^0 \to J/\psi K^+\pi^-$ data as well as the average uncalibrated mistag estimation. The uncertainties are statistical.

Year	p_0	p_1	Δp_0	Δp_1	$\bar{\eta}$
2016	0.4146 ± 0.0012	0.896 ± 0.012	0.0006 ± 0.0017	-0.189 ± 0.018	0.4056
2017	0.4124 ± 0.0012	0.922 ± 0.012	-0.0016 ± 0.0017	-0.234 ± 0.018	0.4044
2018	0.4128 ± 0.0011	0.926 ± 0.011	-0.0021 ± 0.0016	-0.182 ± 0.016	0.4038

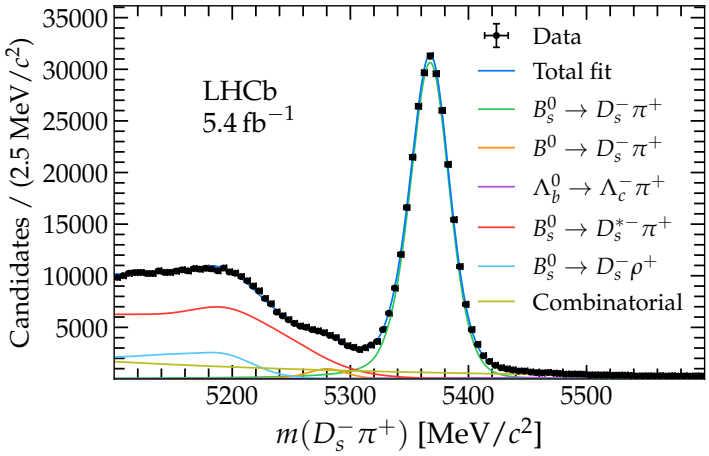

Figure 6: Invariant-mass distribution of $B_s^0 \to D_s^- \pi^+$ candidates in the combined data sample with the result of the fit also shown.

partially reconstructed and misidentified b-hadron decays are free to vary in the fit. In the second step, a fit is performed in the narrower mass window $[5300, 5600]$ MeV/c^2 to extract the *sWeights*. Here, all parameters are fixed to the results of the first fit, except for the signal and total background yields, which are allowed to vary. The resulting $B_s^0 \to D_s^- \pi^+$ signal yields are 85×10^3, 87×10^3 and 101×10^3 for 2016, 2017 and 2018, respectively.

In the fit to the decay-time distribution, the decay-time acceptance is modelled, as in the case of $B^0 \to J/\psi K^+\pi^-$ decays, with cubic splines. The cubic spline parameters are free in the fit to the data.

The B_s^0 decay-time resolution, σ_t, is calibrated in a fit to the decay-time distribution of background-subtracted prompt $D_s^- \to K^+K^-\pi^-$ decays produced from pp collisions combined with an opposite-charge track. These are selected in the same way as the $B_s^0 \to D_s^- \pi^+$ decays, except for the requirement on the B_s^0 candidate decay time, which is not imposed. An unbinned maximum-likelihood fit to the decay-time distribution of the candidates is performed in each of ten σ_t bins using a PDF proportional to

$$f_{\text{sig}} \cdot \left[(f_{\text{prompt}} \delta(t) + f_{ll} e^{-t/\tau_2}) * G(t - t') \right] + f_{\text{wpv}} e^{-|t|/\tau_1}, \tag{8}$$

where the resolution function $G(t)$ consists of the sum of two Gaussian functions with a common mean, two standard deviations σ_1 and σ_2 and a relative fraction f_1 [33]. The prompt signal component, contributing with a fraction f_{prompt}, is assumed to have zero lifetime and is modelled with a Dirac δ distribution. In addition, two components with

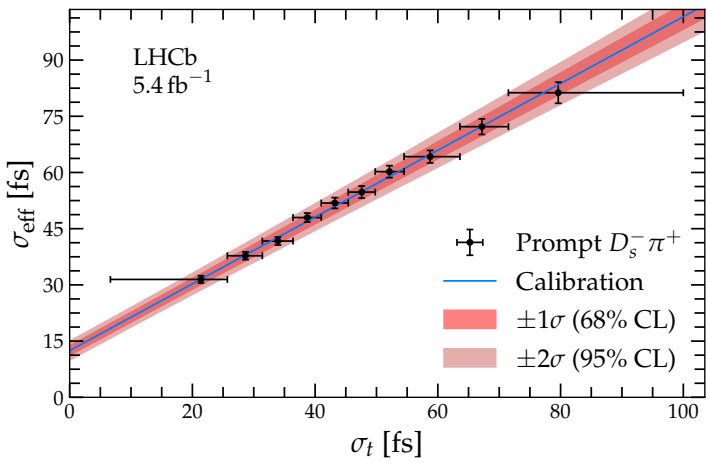

Figure 7: Measured effective decay-time resolution $\sigma_{\rm eff}$ as a function of the reconstructed decay-time resolution σ_t in prompt $D_s^- \pi^+$ data.

finite lifetimes, τ_1 and τ_2, and fractions $f_{\rm wpv} \equiv (1 - f_{\rm sig})$ and $f_{ll} \equiv (1 - f_{\rm prompt})$ are modelled with exponential functions. The exponential functions represent prompt D_s^- candidates associated to a wrong PV, and D_s^- mesons originating from decays of heavier particles. The standard deviations of the two Gaussian components in $G(t - t')$ are combined into a single effective resolution, $\sigma_{\rm eff}$, which yields the same dilution of the B_s^0-meson oscillation amplitude, D_t, as the resolution model $G(t - t')$ in Eq. 8. This effective resolution is computed according to

$$\begin{aligned} D_t &= f_1 e^{-\sigma_1^2 \Delta m_s^2/2} + (1 - f_1) e^{-\sigma_2^2 \Delta m_s^2/2}, \\ \sigma_{\rm eff} &= \sqrt{-2 \ln D_t} / \Delta m_s. \end{aligned} \tag{9}$$

Differences in the selection between the prompt $D_s^- \pi^+$ calibration sample and the $B_s^0 \to D_s^- \pi^+$ sample are accounted for by scaling σ_t according to differences among the corresponding simulated samples. A χ^2 fit is performed in bins of the measured decay-time resolution σ_t assuming a linear dependency of $\sigma_{\rm eff}$ on σ_t. The results are shown in Fig. 7. The results of this fit are used as a per-candidate conditional variable, which are converted to the standard deviation of the Gaussian decay-time resolution model in Eq. 5.

A maximum-likelihood fit to the background-subtracted decay time of the $B_s^0 \to D_s^- \pi^+$ sample is performed. The fit results are shown in Fig. 8. The resulting IFT calibration function is shown in Fig. 9. The calibration parameters are summarised in Table 2. The correlations between them do not exceed 5%.

5 Performance

The performance of the IFT algorithm after calibration is evaluated on data and compared to the performance achieved by combining the existing LHCb flavour-tagging algorithms, the OS and the SS taggers. The five OS taggers are used to compare both the B^0 and the B_s^0 taggers. On the other hand, given the different hadronisation processes for B^0 and B_s^0

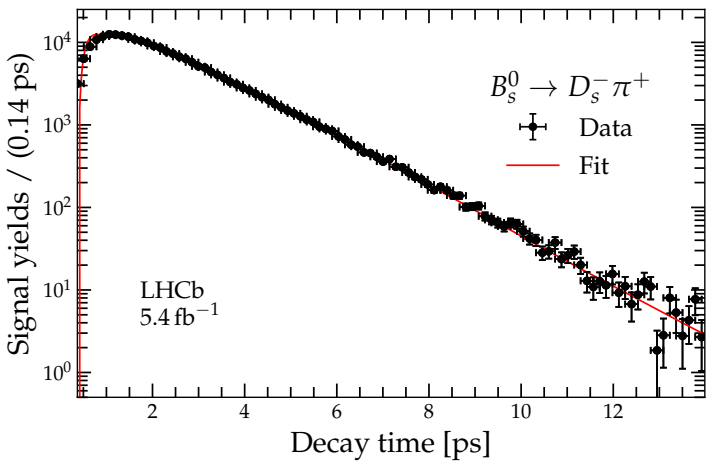

Figure 8: Background-subtracted decay-time distribution of $B_s^0 \to D_s^- \pi^+$ candidates in the data sample combined across all data-taking years and initial and final flavours, together with the fit result.

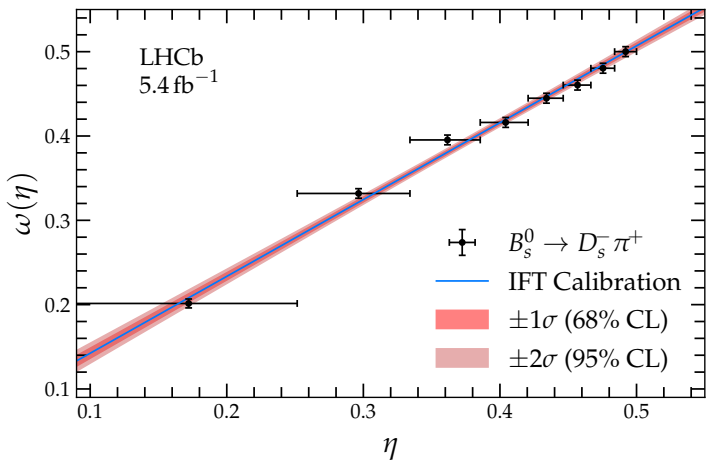

Figure 9: Distribution of the measured mistag fraction ω as a function of the mistag probability η in $B_s^0 \to D_s^- \pi^+$ data. The data points are obtained by performing a decay-time fit in each η bin and extracting the fraction of mistagged events.

Table 2: Results of the unbinned decay-time fit for the IFT calibration parameters in $B_s^0 \to D_s^- \pi^+$ data as well as the average uncalibrated mistag estimation. The uncertainties are statistical.

Year	p_0	p_1	Δp_0	Δp_1	$\bar{\eta}$
2016	0.4038 ± 0.0041	0.954 ± 0.037	0.0147 ± 0.0037	-0.083 ± 0.035	0.3872
2017	0.4014 ± 0.0036	0.877 ± 0.032	0.0062 ± 0.0036	0.027 ± 0.034	0.3871
2018	0.4022 ± 0.0033	0.880 ± 0.030	0.0123 ± 0.0034	-0.046 ± 0.031	0.3864

mesons, the SS taggers used in the comparison are based on pions and protons for B^0 and on kaons for B_s^0 decays.

The combination of multiple tag decisions, d_i, and mistag estimations, η_i, is obtained by calculating the probability of the signal candidate to contain a b or a $\bar{b}$ quark, denoted as $P(b)$ and $P(\bar{b})$,

$$P(b) = \frac{p(b)}{p(b) + p(\bar{b})}, \quad P(\bar{b}) = 1 - P(b), \tag{10}$$

where the probabilities $p(b)$ and $p(\bar{b})$ for uncorrelated tagging decisions are defined as

$$\begin{aligned} p(b) &= \prod_i \left(\frac{1 + d_i}{2} - d_i(1 - \eta_i) \right), \\ p(\bar{b}) &= \prod_i \left(\frac{1 - d_i}{2} + d_i(1 - \eta_i) \right). \end{aligned} \tag{11}$$

The combined tagging decision and the combined mistag estimate are given by

$$\begin{aligned} d_{\text{comb}} &= \text{sign}(P(\bar{b}) - P(b)), \\ \eta_{\text{comb}} &= 1 - \max(P(b), P(\bar{b})). \end{aligned} \tag{12}$$

The combination of the SS and OS taggers proceeds in three steps. First, the individual OS taggers are combined into a single OS decision and mistag estimate. Independently of the OS taggers, the two SS taggers used in the B^0 classifier are combined into a single SS decision and mistag estimate. Subsequently, the OS combination mistag estimate and, in the case of the B^0 classifier, the SS combination or, in the case of the B_s^0 classifier, the SS kaon mistag estimate, are calibrated according to Eqs. 7. In the final step, the calibrated OS combination and the SS combination or SS kaon are again combined into a single decision and mistag estimation, which is further calibrated according to Eqs. 7. Performing the calibration after combining the taggers is essential to properly account for potential correlations between them, which could otherwise bias the resulting mistag. The calibrations are verified to be in agreement with those obtained using a dedicated flavour-tagging calibration software package `lhcb-ftcalib` [34].

5.1 Performance of the B^0 classifier

The performance of the B^0 classifier on data is determined for two decay modes, $B^0 \to J/\psi K^+\pi^-$ and $B^0 \to J/\psi K_S^0$ decays. It is compared to the performances of the SS and OS taggers and their combination. The performances on the $B^0 \to J/\psi K^+\pi^-$ samples are summarised in Table 3. A relative tagging power increase of at least 35% over the combination of SS and OS taggers is observed.

The IFT tagging power on $B^0 \to J/\psi K^+\pi^-$ data in relation to the tagging decision of the SS and OS taggers across all years is shown in Table 4. For this study, the dataset is divided into five subsets based on the tagging decisions: events with only an SS tagger decision, only an OS tagger decision, both SS and OS tagger decisions, at least one tagger decision (SS or OS), and events with neither SS nor OS tagger decisions. A recalibration is then performed separately on each of these subsets using the full dataset spanning all years. Since events with $\omega > 0.5$ are treated as untagged, recalibrating each subset independently results in total efficiencies and performances that differ from those computed on the full

Table 3: Performances on $B^0 \to J/\psi K^+\pi^-$ data for the combination of SS and OS taggers versus the IFT. The uncertainties are statistical.

Year	Tagger	$\varepsilon_{\text{tag}}(\%)$	$\langle D^2 \rangle$	$\varepsilon_{\text{tag}}\langle D^2 \rangle(\%)$
2016	SS and OS	87.030 ± 0.058	0.0466 ± 0.0010	4.05 ± 0.09
	IFT	95.789 ± 0.035	0.0582 ± 0.0011	5.58 ± 0.10
2017	SS and OS	87.208 ± 0.058	0.0485 ± 0.0010	4.23 ± 0.09
	IFT	95.024 ± 0.038	0.0617 ± 0.0011	5.87 ± 0.10
2018	SS and OS	87.631 ± 0.052	0.0493 ± 0.0010	4.32 ± 0.09
	IFT	95.172 ± 0.034	0.0615 ± 0.0010	5.85 ± 0.10

Table 4: Performance of the IFT on $B^0 \to J/\psi K^+\pi^-$ data for all years, evaluated separately for events with only SS tagger decisions, only OS tagger decisions, both SS and OS tagger decisions, at least one tagger decision (SS or OS), and no tagger decision from either SS or OS taggers.

Configuration	$\varepsilon_{\text{tag}}(\%)$	$\langle D^2 \rangle$	$\varepsilon_{\text{tag}}\langle D^2 \rangle(\%)$
only SS	51.79 ± 0.05	0.0343 ± 0.0008	1.77 ± 0.03
only OS	4.90 ± 0.02	0.1239 ± 0.0031	0.61 ± 0.02
SS and OS	28.75 ± 0.05	0.1126 ± 0.0013	3.24 ± 0.04
SS or OS	85.06 ± 0.03	0.0664 ± 0.0006	5.64 ± 0.06
neither	10.93 ± 0.02	0.0128 ± 0.0020	0.14 ± 0.01

dataset. The absolute tagging power obtained in events not tagged by either the SS or OS taggers represents only a small fraction of the overall improvement in tagging power achieved by the IFT. In contrast, the IFT tagging power for events tagged either by the SS or the OS taggers, accounts for the dominant share of the improvement with respect to using the SS and OS taggers alone. This indicates that the improvement in the tagging power is driven by additional information the IFT uses in events tagged by SS and OS.

The B^0 IFT was developed using simulated $B^0 \to J/\psi K^{*0}$ decays. To assess whether its performance improvement over the current flavour-tagging algorithm is also observed in other decay modes, the calibration from the control channel is adapted to the $B^0 \to J/\psi K^0_S$ decay in data, and the tagging power is subsequently measured. Decays of $K^0_S \to \pi^+\pi^-$ are reconstructed from two tracks forming a good-quality vertex in two different categories: the first one consists of K^0_S mesons that decay within the acceptance of the vertex detector, and the second contains K^0_S that decay outside of the vertex detector. The selection criteria are based on the latest measurement of $\sin(2\beta)$ [3], though they are simplified by not applying a full multivariate selection. The resulting signal yields are 29×10^3, 30×10^3 and 34×10^3 for 2016, 2017 and 2018, respectively.

The mistag probability for all taggers is calibrated using $B^0 \to J/\psi K^+\pi^-$ decays which are weighted so that the distributions of the p_T and pseudorapidity of the signal B meson, the number of tracks and the number of PVs match those in $B^0 \to J/\psi K^0_S$ data. Table 5 compares the calibrated tagging power across all years for the SS and OS tagger combination and the IFT on $B^0 \to J/\psi K^0_S$ data. Interestingly, the relative improvement over the SS and OS taggers is greater than in $B^0 \to J/\psi K^+\pi^-$ data. This is due to differences in tagging efficiency, as shown in Tables 3 and 5. In the recent

Table 5: Performances evaluated for $B^0 \to J/\psi K^0_S$ data for the combination of SS and OS taggers and the IFT. The uncertainties are statistical.

Year	Tagger	$\varepsilon_{\text{tag}}(\%)$	$\langle D^2 \rangle$	$\varepsilon_{\text{tag}}\langle D^2 \rangle(\%)$
2016	SS and OS	69.18 ± 0.35	0.0473 ± 0.0011	3.27 ± 0.08
	IFT	95.42 ± 0.16	0.0563 ± 0.0012	5.37 ± 0.12
2017	SS and OS	68.65 ± 0.34	0.0482 ± 0.0011	3.31 ± 0.08
	IFT	98.53 ± 0.09	0.0571 ± 0.0012	5.63 ± 0.12
2018	SS and OS	69.58 ± 0.31	0.0487 ± 0.0010	3.38 ± 0.07
	IFT	96.41 ± 0.13	0.0573 ± 0.0011	5.52 ± 0.11

$\sin(2\beta)$ measurement, which uses a more refined candidate selection, the tagging efficiency is $(85.34 \pm 0.05)\%$, similar to $B^0 \to J/\psi K^+\pi^-$ decays, see Table 3. Differences in the tagging dilution between this study and the $\sin(2\beta)$ measurement are negligible. Therefore, the reduced tagging power of the SS and OS taggers compared to that measurement is attributed to lower tagging efficiency resulting from the simplified signal selection. In contrast, the performance of the IFT remains robust under these changes. By correcting the efficiency to one of the $B^0 \to J/\psi K^0_S$ samples selected as in the $\sin(2\beta)$ measurement to 85%, while keeping the dilution constant, the IFT improvement aligns with that observed in $B^0 \to J/\psi K^+\pi^-$ decays.

5.2 Performance of the B^0_s classifier

The tagging performance of the B^0_s classifier is evaluated on $B^0_s \to D^-_s\pi^+$ and $B^0_s \to J/\psi K^+K^-$ data using the calibration from $B^0_s \to D^-_s\pi^+$ data. The selection is identical to that developed for the ϕ_s measurement [4]. The resulting signal yields are 99×10^3, 103×10^3 and 123×10^3 for 2016, 2017 and 2018, respectively.

An improvement of the IFT over the SS and OS combination at the level of approximately 20% is observed, as shown in Tables 6 and 7. For the performance on $B^0_s \to J/\psi K^+K^-$ data, the IFT is calibrated on $B^0_s \to D^-_s\pi^+$ data weighted so that the distributions of the p_{T} and pseudorapidity of the signal B meson, the number of tracks and the number of PVs match those in $B^0_s \to J/\psi K^+K^-$ data. The difference in absolute tagging power between the two modes, both for the SS and OS combination and for the IFT, is expected. This is mainly due to the different signal B^0_s-meson p_{T} spectra of the two modes (see Sec. 5) and the known dependency of the SS tagger performance on the B-meson p_{T} [8]. The tagging power on $B^0_s \to D^-_s\pi^+$ data in relation to the tagging decision of the SS and OS taggers is shown in Table 8. These values are obtained using the same method as for $B^0 \to J/\psi K^+\pi^-$ decays and exhibit similar behaviour.

The impact of the IFT on the precision of the CP-violating phase ϕ_s is measured in a blinded fit to $B^0_s \to J/\psi K^+K^-$ data, performed analogously to the ϕ_s analysis [4]. The uncertainties on the calibration parameters are constrained by applying Gaussian penalty terms in the fit based on their respective statistical and systematic effects. The use of the IFT reduces the uncertainty on ϕ_s by approximately 10% compared to the combination of SS and OS taggers. This result is consistent with the observed 20% improvement in tagging power, which corresponds to an effective increase in the data sample size by a factor of 1.2, leading to an expected uncertainty reduction proportional to the square root

Table 6: Performances on $B_s^0 \to D_s^- \pi^+$ data for the combination of SS and OS taggers and the IFT. The uncertainties are statistical.

Year	Tagger	$\varepsilon_{\text{tag}}(\%)$	$\langle D^2 \rangle$	$\varepsilon_{\text{tag}}\langle D^2 \rangle(\%)$
2016	SS and OS	73.81 ± 0.16	0.0877 ± 0.0054	6.47 ± 0.40
	IFT	87.97 ± 0.13	0.0882 ± 0.0050	7.76 ± 0.44
2017	SS and OS	79.05 ± 0.15	0.0758 ± 0.0043	5.99 ± 0.34
	IFT	96.87 ± 0.06	0.0747 ± 0.0038	7.23 ± 0.37
2018	SS and OS	74.34 ± 0.15	0.0819 ± 0.0042	6.09 ± 0.31
	IFT	95.49 ± 0.07	0.0760 ± 0.0036	7.25 ± 0.34

Table 7: Performances evaluated for $B_s^0 \to J/\psi K^+ K^-$ data for the combination of SS and OS taggers and the IFT. The uncertainties are statistical.

Year	Tagger	$\varepsilon_{\text{tag}}(\%)$	$\langle D^2 \rangle$	$\varepsilon_{\text{tag}}\langle D^2 \rangle(\%)$
2016	SS and OS	74.91 ± 0.14	0.0623 ± 0.0039	4.67 ± 0.29
	IFT	91.18 ± 0.09	0.0609 ± 0.0035	5.55 ± 0.32
2017	SS and OS	76.18 ± 0.14	0.0582 ± 0.0034	4.44 ± 0.26
	IFT	93.18 ± 0.08	0.0578 ± 0.0030	5.38 ± 0.28
2018	SS and OS	72.31 ± 0.13	0.0628 ± 0.0033	4.54 ± 0.24
	IFT	90.32 ± 0.09	0.0604 ± 0.0029	5.46 ± 0.26

of the factor of increase.

5.3 Performance trends

A possible dependence of the IFT calibration parameters on kinematic and event-level observables of the sample is checked using $B^0 \to J/\psi K^+ \pi^-$ and $B_s^0 \to D_s^- \pi^+$ data by repeating the calibration in bins of p_{T} and pseudorapidity of the signal B meson, the track multiplicity and the number of PVs. The trends in the IFT performance, shown in Figs. 10 and 11, are similar to those observed for the SS and OS tagger combination. The tagging power increases as a function of the transverse momentum of the signal B-meson candidate, which is understood to be driven by the SS tracks. The mistag probability of

Table 8: Performance of the IFT on $B_s^0 \to D_s^- \pi^+$ data for all years, evaluated separately for events with only SS tagger decisions, only OS tagger decisions, both SS and OS tagger decisions, at least one tagger decision (SS or OS), and no tagger decision from either SS or OS taggers.

Configuration	$\varepsilon_{\text{tag}}(\%)$	$\langle D^2 \rangle$	$\varepsilon_{\text{tag}}\langle D^2 \rangle(\%)$
only SS	41.24 ± 0.10	0.0475 ± 0.0029	1.96 ± 0.03
only OS	11.41 ± 0.07	0.1266 ± 0.0058	1.44 ± 0.09
SS and OS	26.36 ± 0.09	0.1498 ± 0.0037	3.95 ± 0.15
SS or OS	77.54 ± 0.09	0.0939 ± 0.0022	7.28 ± 0.20
neither	18.59 ± 0.08	0.0092 ± 0.0045	0.17 ± 0.10

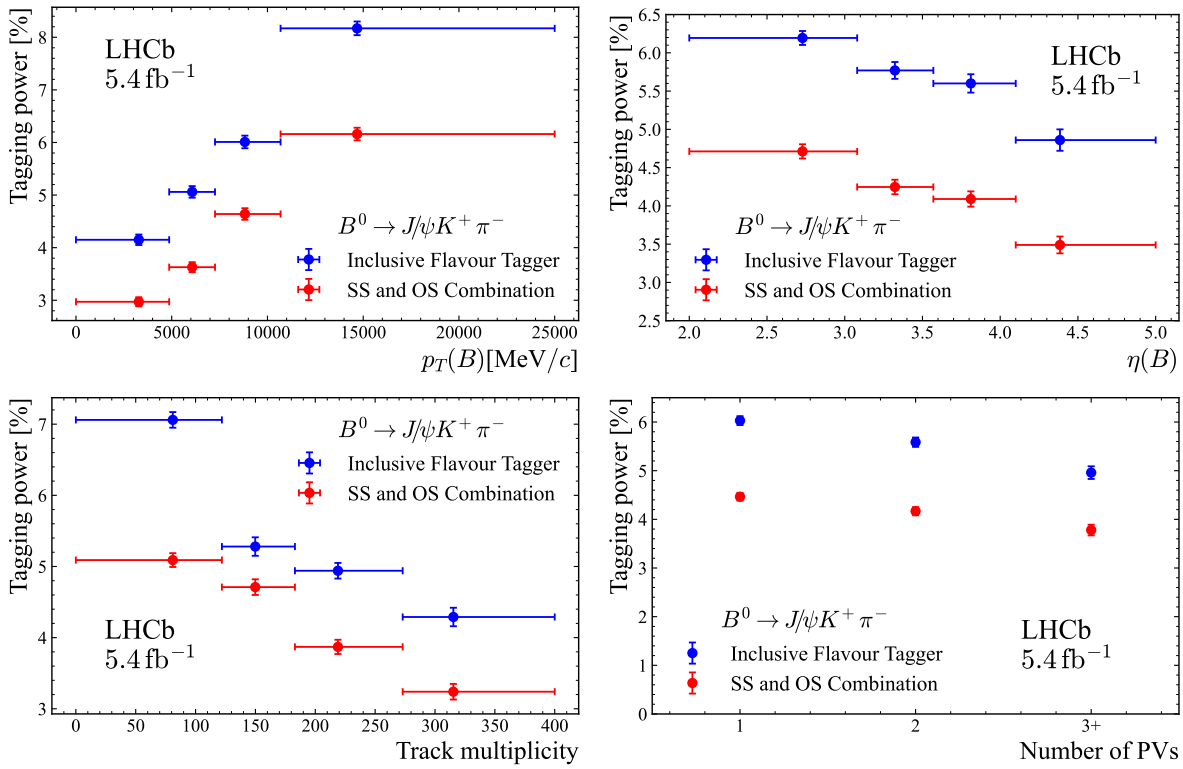

Figure 10: Performance of the IFT and the SS and OS tagger combination in $B^0 \to J/\psi K^+\pi^-$ data as a function of the signal B-meson (top left) p_{T} and (top right) pseudorapidity, (bottom left) the track multiplicity and (bottom right) the number of PVs.

the SS tagger decreases with p_{T} since the number of random tracks decreases at high p_{T}, while the tagging power of the OS tagger remains nearly constant. In the B^0 sample, the tagging power decreases with increasing pseudorapidity, mainly driven by the SS tracks and an inverse correlation of the pseudorapidity with p_{T}. No clear trend is observed in the B_s^0 sample where the statistical uncertainty is also significantly larger. In both samples, higher track multiplicities lead to a lower performance as a consequence of the higher probability of using a wrong track for tagging and therefore a higher mistag rate. Furthermore, the tagging power decreases with an increasing number of PVs, primarily driven by the incorrect association of tracks to the opposite-side hadron as well as the increased track multiplicity which is highly correlated to the number of PVs. In both modes, the calibration parameters in each bin of the studied variables differ by less than two standard deviations from the expected constant value.

6 Validation and systematic uncertainty studies

Validation studies are performed on simulated $B_s^0 \to J/\psi\phi$ decays to assess possible biases on CP-violating observables introduced by the IFT algorithm. The model is first trained and then applied to a statistically independent simulated sample that was not used for training. A fit for the determination of the CP-violating phase ϕ_s is performed on these samples, using the efficiencies and acceptances from the ϕ_s analysis [4]. The fit results are

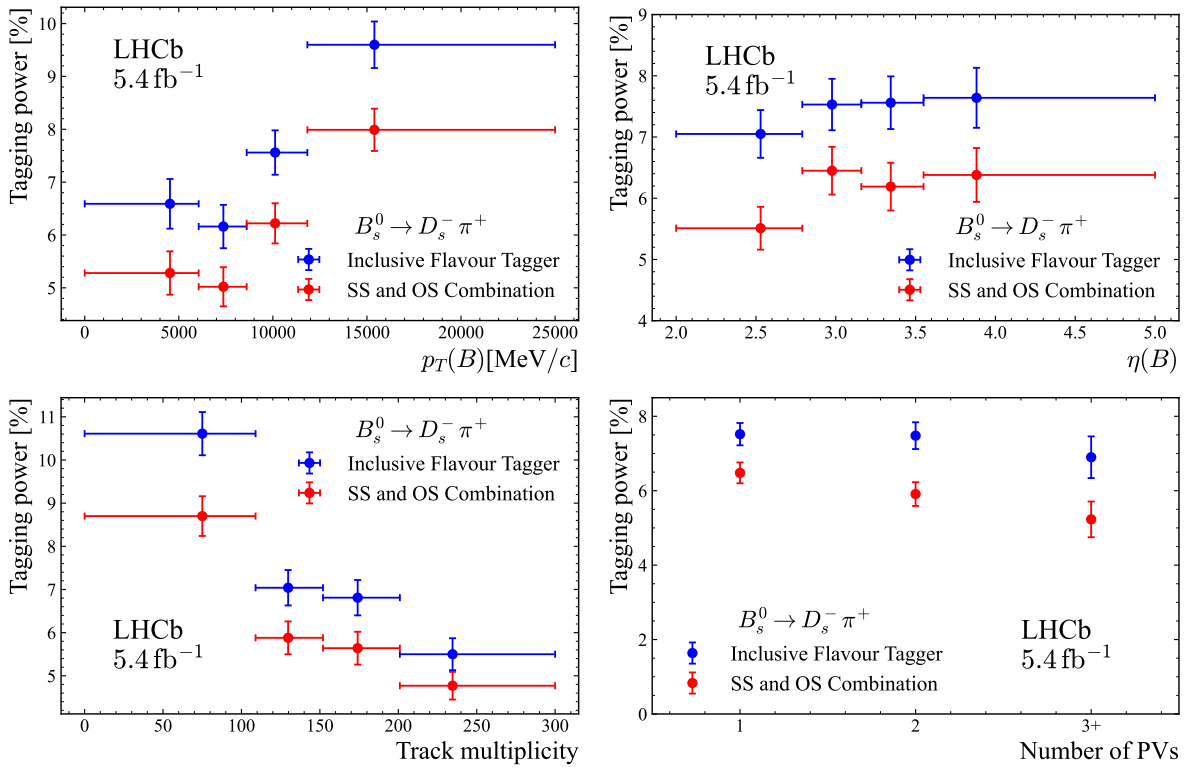

Figure 11: Performance of the IFT and the SS and OS tagger combination in $B_s^0 \to D_s^- \pi^+$ data as a function of the signal B-meson (top left) p_{T} and (top right) pseudorapidity, (bottom left) the track multiplicity and (bottom right) the number of PVs.

in agreement with the generated values for ϕ_s.

The portability of the mistag calibration between calibration and signal decay channels is studied as a potential source of a systematic uncertainty. This effect is studied separately for the B^0 and B_s^0 IFT classifiers. For the B^0 classifier, it is evaluated by comparing the calibration parameters from a fit to simulated $B^0 \to J/\psi K^{*0}$ and $B^0 \to J/\psi K_{\mathrm{S}}^0$ decays, while for the B_s^0 classifier, it is assessed using simulated $B_s^0 \to D_s^- \pi^+$ and $B_s^0 \to J/\psi \phi$ decays. In both cases, the former is the control channel, while the latter is the physics channel.

In this study, $B^0 \to J/\psi K^+ \pi^-$ ($B_s^0 \to D_s^- \pi^+$) decays are weighted so that the distributions of the p_{T} and pseudorapidity of the signal B meson, as well as the number of tracks and PVs, match those in $B^0 \to J/\psi K_{\mathrm{S}}^0$ ($B_s^0 \to J/\psi \phi$) decays. Each decay channel is calibrated independently using information on the generated flavour of the B meson.

For the B^0 classifier, the differences between the calibration parameters of the $B^0 \to J/\psi K^+ \pi^-$ and $B^0 \to J/\psi K_{\mathrm{S}}^0$ simulated decays are comparable to their statistical uncertainties. This applies to both the differences observed in the SS and OS tagger combination and in the IFT. The differences are also comparable to the statistical uncertainties of the calibration parameters observed in $B^0 \to J/\psi K^+ \pi^-$ data.

For the B_s^0 classifier, the differences between the calibration parameters of the $B^0 \to J/\psi \phi$ and the $B_s^0 \to D_s^- \pi^+$ simulated decays are well below the statistical uncertainties, both in simulation and in data, for the SS and OS tagger combination as well

as for the IFT. Additionally, for both the B^0 and B_s^0 classifiers the differences are found to remain stable under retraining of the IFT neural networks.

7 Conclusion

A new algorithm, IFT, is developed to determine the flavour at production of neutral B mesons in pp collisions utilising all tracks from the collision. It is trained separately for B^0 and B_s^0 mesons using the DeepSets neural network. The classifier outputs are calibrated using $B^0 \to J/\psi K^+\pi^-$ and $B_s^0 \to D_s^-\pi^+$ decays collected by the LHCb experiment in pp collisions at 13 TeV. The IFT algorithm is validated on data and simulation and its performance is found to depend on the kinematic variables of the B meson, and event variables such as track and PV multiplicity, in the same way as the combination of the SS and OS taggers used so far at the LHCb experiment. The IFT algorithm provides a tagging power that is greater than the combination of SS and OS taggers by a relative 35% for B^0 mesons and 20% for B_s^0 mesons. This translates into an expected reduction of the statistical uncertainty on the CP-violating parameters by approximately 15% and 10%, respectively.

Acknowledgements

We express our gratitude to our colleagues in the CERN accelerator departments for the excellent performance of the LHC. We thank the technical and administrative staff at the LHCb institutes. We acknowledge support from CERN and from the national agencies: ARC (Australia); CAPES, CNPq, FAPERJ and FINEP (Brazil); MOST and NSFC (China); CNRS/IN2P3 (France); BMFTR, DFG and MPG (Germany); INFN (Italy); NWO (Netherlands); MNiSW and NCN (Poland); MCID/IFA (Romania); MICIU and AEI (Spain); SNSF and SER (Switzerland); NASU (Ukraine); STFC (United Kingdom); DOE NP and NSF (USA). We acknowledge the computing resources that are provided by ARDC (Australia), CBPF (Brazil), CERN, IHEP and LZU (China), IN2P3 (France), KIT and DESY (Germany), INFN (Italy), SURF (Netherlands), Polish WLCG (Poland), IFIN-HH (Romania), PIC (Spain), CSCS (Switzerland), and GridPP (United Kingdom). We are indebted to the communities behind the multiple open-source software packages on which we depend. Individual groups or members have received support from Key Research Program of Frontier Sciences of CAS, CAS PIFI, CAS CCEPP, Fundamental Research Funds for the Central Universities, and Sci. & Tech. Program of Guangzhou (China); Minciencias (Colombia); EPLANET, Marie Skłodowska-Curie Actions, ERC and NextGenerationEU (European Union); A*MIDEX, ANR, IPhU and Labex P2IO, and Région Auvergne-Rhône-Alpes (France); Alexander-von-Humboldt Foundation (Germany); ICSC (Italy); Severo Ochoa and María de Maeztu Units of Excellence, GVA, XuntaGal, GENCAT, InTalent-Inditex and Prog. Atracción Talento CM (Spain); SRC (Sweden); the Leverhulme Trust, the Royal Society and UKRI (United Kingdom).

References

[1] LHCb collaboration, R. Aaij *et al.*, *A precise measurement of the B^0 meson oscillation frequency*, Eur. Phys. J. **C76** (2016) 412, arXiv:1604.03475.

[2] LHCb collaboration, R. Aaij *et al.*, *Precise determination of the B_s^0-$\overline{B}_s^0$ oscillation frequency*, Nature Physics **18** (2022) 1, arXiv:2104.04421.

[3] LHCb collaboration, R. Aaij *et al.*, *Measurement of CP violation in $B^0 \to \psi(\to \ell^+\ell^-)K_S^0(\to \pi^+\pi^-)$ decays*, Phys. Rev. Lett. **132** (2024) 021801, arXiv:2309.09728.

[4] LHCb collaboration, R. Aaij *et al.*, *Improved measurement of CP violation parameters in $B_s^0 \to J/\psi K^+K^-$ decays in the vicinity of the $\phi(1020)$ resonance*, Phys. Rev. Lett. **132** (2024) 051802, arXiv:2308.01468.

[5] LHCb collaboration, R. Aaij *et al.*, *B flavour tagging using charm decays at the LHCb experiment*, JINST **10** (2015) P10005, arXiv:1507.07892.

[6] LHCb collaboration, R. Aaij *et al.*, *Opposite-side flavour tagging of B mesons at the LHCb experiment*, Eur. Phys. J. **C72** (2012) 2022, arXiv:1202.4979.

[7] LHCb collaboration, R. Aaij *et al.*, *A new algorithm for identifying the flavour of B_s^0 mesons at LHCb*, JINST **11** (2016) P05010, arXiv:1602.07252.

[8] LHCb collaboration, R. Aaij *et al.*, *New algorithms for identifying the flavour of B^0 mesons using pions and protons*, Eur. Phys. J. **C77** (2017) 238, arXiv:1610.06019.

[9] T. Likhomanenko, D. Derkach, and A. Rogozhnikov, *Inclusive flavour tagging algorithm*, J. Phys. Conf. Ser. **762** (2016) 012045, arXiv:1705.08707.

[10] Belle II collaboration, I. Adachi *et al.*, *New graph-neural-network flavor tagger for Belle II and measurement of $\sin 2\phi_1$ in $B^0 \to J/\psi K_S^0$ decays*, Phys. Rev. **D110** (2024) 012001, arXiv:2402.17260.

[11] M. Zaheer *et al.*, *Deep sets*, NIPS'17, (Red Hook, NY, USA), 3394–3404, Curran Associates Inc., 2017, arXiv:1703.06114.

[12] LHCb collaboration, A. A. Alves Jr. *et al.*, *The LHCb detector at the LHC*, JINST **3** (2008) S08005.

[13] LHCb collaboration, R. Aaij *et al.*, *LHCb detector performance*, Int. J. Mod. Phys. **A30** (2015) 1530022, arXiv:1412.6352.

[14] R. Aaij *et al.*, *Performance of the LHCb Vertex Locator*, JINST **9** (2014) P09007, arXiv:1405.7808.

[15] P. d'Argent *et al.*, *Improved performance of the LHCb Outer Tracker in LHC Run 2*, JINST **12** (2017) P11016, arXiv:1708.00819.

[16] M. Adinolfi *et al.*, *Performance of the LHCb RICH detector at the LHC*, Eur. Phys. J. **C73** (2013) 2431, arXiv:1211.6759.

[17] A. A. Alves Jr. *et al.*, *Performance of the LHCb muon system*, JINST **8** (2013) P02022, arXiv:1211.1346.

[18] R. Aaij *et al.*, *The LHCb trigger and its performance in 2011*, JINST **8** (2013) P04022, arXiv:1211.3055.

[19] T. Sjöstrand, S. Mrenna, and P. Skands, *A brief introduction to PYTHIA 8.1*, Comput. Phys. Commun. **178** (2008) 852, arXiv:0710.3820; T. Sjöstrand, S. Mrenna, and P. Skands, *PYTHIA 6.4 physics and manual*, JHEP **05** (2006) 026, arXiv:hep-ph/0603175.

[20] I. Belyaev *et al.*, *Handling of the generation of primary events in Gauss, the LHCb simulation framework*, J. Phys. Conf. Ser. **331** (2011) 032047.

[21] D. J. Lange, *The EvtGen particle decay simulation package*, Nucl. Instrum. Meth. **A462** (2001) 152.

[22] N. Davidson, T. Przedzinski, and Z. Was, *PHOTOS interface in C++: Technical and physics documentation*, Comput. Phys. Commun. **199** (2016) 86, arXiv:1011.0937.

[23] Geant4 collaboration, J. Allison *et al.*, *Geant4 developments and applications*, IEEE Trans. Nucl. Sci. **53** (2006) 270; Geant4 collaboration, S. Agostinelli *et al.*, *Geant4: A simulation toolkit*, Nucl. Instrum. Meth. **A506** (2003) 250.

[24] M. Clemencic *et al.*, *The LHCb simulation application, Gauss: Design, evolution and experience*, J. Phys. Conf. Ser. **331** (2011) 032023.

[25] CMS collaboration, Hayrapetyan, Aram *et al.* , *Evidence for CP violation and measurement of CP-violating parameters in $B_s^0 \to J/\psi\,\phi(1020)$ decays in pp collisions at $\sqrt{s} = 13$ TeV*, arXiv:2412.19952.

[26] L. Breiman, J. H. Friedman, R. A. Olshen, and C. J. Stone, *Classification and regression trees*, Wadsworth international group, Belmont, California, USA, 1984.

[27] Y. Freund and R. E. Schapire, *A decision-theoretic generalization of on-line learning and an application to boosting*, J. Comput. Syst. Sci. **55** (1997) 119.

[28] T. Chen and C. Guestrin, *XGBoost: A scalable tree boosting system*, in *Proceedings of the 22nd ACM SIGKDD International Conference on Knowledge Discovery and Data Mining*, KDD '16, (New York, NY, USA), 785–794, ACM, 2016.

[29] Particle Data Group, S. Navas *et al.*, *Review of particle physics*, Phys. Rev. **D110** (2024) 030001.

[30] Heavy Flavor Averaging Group, S. Banerjee *et al.*, *Averages of b-hadron, c-hadron, and τ-lepton properties as of 2023*, arXiv:2411.18639, updated results and plots available at https://hflav.web.cern.ch.

[31] M. Pivk and F. R. Le Diberder, *sPlot: A statistical tool to unfold data distributions*, Nucl. Instrum. Meth. **A555** (2005) 356, arXiv:physics/0402083.

[32] D. Martínez Santos and F. Dupertuis, *Mass distributions marginalized over per-event errors*, Nucl. Instrum. Meth. **A764** (2014) 150, arXiv:1312.5000.

[33] LHCb collaboration, R. Aaij *et al.*, *Updated measurement of time-dependent CP-violating observables in $B_s^0 \to J/\psi K^+K^-$ decays*, Eur. Phys. J. **C79** (2019) 706, Erratum ibid. **C80** (2020) 601, arXiv:1906.08356.

[34] Q. Führing and V. Jevtić, *lhcb-ftcalib: A software package for the calibration of flavour-tagged LHCb data*, 2024. doi: 10.5281/zenodo.12156328.

LHCb collaboration

R. Aaij[38], A.S.W. Abdelmotteleb[57], C. Abellan Beteta[51], F. Abudinén[57], T. Ackernley[61], A. A. Adefisoye[69], B. Adeva[47], M. Adinolfi[55], P. Adlarson[85], C. Agapopoulou[14], C.A. Aidala[87], Z. Ajaltouni[11], S. Akar[11], K. Akiba[38], P. Albicocco[28], J. Albrecht[19,g], R. Aleksiejunas[80], F. Alessio[49], P. Alvarez Cartelle[56], R. Amalric[16], S. Amato[3], J.L. Amey[55], Y. Amhis[14], L. An[6], L. Anderlini[27], M. Andersson[51], P. Andreola[51], M. Andreotti[26], S. Andres Estrada[84], A. Anelli[31,p,49], D. Ao[7], F. Archilli[37,w], Z Areg[69], M. Argenton[26], S. Arguedas Cuendis[9,49], A. Artamonov[44], M. Artuso[69], E. Aslanides[13], R. Ataíde Da Silva[50], M. Atzeni[65], B. Audurier[12], J. A. Authier[15], D. Bacher[64], I. Bachiller Perea[50], S. Bachmann[22], M. Bachmayer[50], J.J. Back[57], P. Baladron Rodriguez[47], V. Balagura[15], A. Balboni[26], W. Baldini[26], Z. Baldwin[78], L. Balzani[19], H. Bao[7], J. Baptista de Souza Leite[61], C. Barbero Pretel[47,12], M. Barbetti[27], I. R. Barbosa[70], R.J. Barlow[63], M. Barnyakov[25], S. Barsuk[14], W. Barter[59], J. Bartz[69], S. Bashir[40], B. Batsukh[5], P. B. Battista[14], A. Bay[50], A. Beck[65], M. Becker[19], F. Bedeschi[35], I.B. Bediaga[2], N. A. Behling[19], S. Belin[47], A. Bellavista[25], K. Belous[44], I. Belov[29], I. Belyaev[36], G. Benane[13], G. Bencivenni[28], E. Ben-Haim[16], A. Berezhnoy[44], R. Bernet[51], S. Bernet Andres[46], A. Bertolin[33], C. Betancourt[51], F. Betti[59], J. Bex[56], Ia. Bezshyiko[51], O. Bezshyyko[86], J. Bhom[41], M.S. Bieker[18], N.V. Biesuz[26], P. Billoir[16], A. Biolchini[38], M. Birch[62], F.C.R. Bishop[10], A. Bitadze[63], A. Bizzeti[27,q], T. Blake[57,c], F. Blanc[50], J.E. Blank[19], S. Blusk[69], V. Bocharnikov[44], J.A. Boelhauve[19], O. Boente Garcia[15], T. Boettcher[68], A. Bohare[59], A. Boldyrev[44], C.S. Bolognani[82], R. Bolzonella[26,m], R. B. Bonacci[1], N. Bondar[44,49], A. Bordelius[49], F. Borgato[33,49], S. Borghi[63], M. Borsato[31,p], J.T. Borsuk[83], E. Bottalico[61], S.A. Bouchiba[50], M. Bovill[64], T.J.V. Bowcock[61], A. Boyer[49], C. Bozzi[26], J. D. Brandenburg[88], A. Brea Rodriguez[50], N. Breer[19], J. Brodzicka[41], A. Brossa Gonzalo[47,†], J. Brown[61], D. Brundu[32], E. Buchanan[59], M. Burgos Marcos[82], A.T. Burke[63], C. Burr[49], J.S. Butter[56], J. Buytaert[49], W. Byczynski[49], S. Cadeddu[32], H. Cai[75], Y. Cai[5], A. Caillet[16], R. Calabrese[26,m], S. Calderon Ramirez[9], L. Calefice[45], S. Cali[28], M. Calvi[31,p], M. Calvo Gomez[46], P. Camargo Magalhaes[2,a], J. I. Cambon Bouzas[47], P. Campana[28], D.H. Campora Perez[82], A.F. Campoverde Quezada[7], S. Capelli[31], M. Caporale[25], L. Capriotti[26], R. Caravaca-Mora[9], A. Carbone[25,k], L. Carcedo Salgado[47], R. Cardinale[29,n], A. Cardini[32], P. Carniti[31], L. Carus[22], A. Casais Vidal[65], R. Caspary[22], G. Casse[61], M. Cattaneo[49], G. Cavallero[26], V. Cavallini[26,m], S. Celani[22], I. Celestino[35,t], S. Cesare[30,o], F. Cesario Laterza Lopes[2], A.J. Chadwick[61], I. Chahrour[87], H. Chang[4,d], M. Charles[16], Ph. Charpentier[49], E. Chatzianagnostou[38], R. Cheaib[79], M. Chefdeville[10], C. Chen[56], J. Chen[50], S. Chen[5], Z. Chen[7], M. Cherif[12], A. Chernov[41], S. Chernyshenko[53], X. Chiotopoulos[82], V. Chobanova[84], M. Chrzaszcz[41], A. Chubykin[44], V. Chulikov[28,36,49], P. Ciambrone[28], X. Cid Vidal[47], G. Ciezarek[49], P. Cifra[38], P.E.L. Clarke[59], M. Clemencic[49], H.V. Cliff[56], J. Closier[49], C. Cocha Toapaxi[22], V. Coco[49], J. Cogan[13], E. Cogneras[11], L. Cojocariu[43], S. Collaviti[50], P. Collins[49], T. Colombo[49], M. Colonna[19], A. Comerma-Montells[45], L. Congedo[24], J. Connaughton[57], A. Contu[32], N. Cooke[60], G. Cordova[35,t], C. Coronel[66], I. Corredoira [12], A. Correia[16], G. Corti[49], J. Cottee Meldrum[55], B. Couturier[49], D.C. Craik[51], M. Cruz Torres[2,h], E. Curras Rivera[50], R. Currie[59], C.L. Da Silva[68], S. Dadabaev[44], L. Dai[72], X. Dai[4], E. Dall'Occo[49], J. Dalseno[84], C. D'Ambrosio[62],

J. Daniel[11], P. d'Argent[24], G. Darze[3], A. Davidson[57], J.E. Davies[63], O. De Aguiar Francisco[63], C. De Angelis[32,l], F. De Benedetti[49], J. de Boer[38], K. De Bruyn[81], S. De Capua[63], M. De Cian[63], U. De Freitas Carneiro Da Graca[2,b], E. De Lucia[28], J.M. De Miranda[2], L. De Paula[3], M. De Serio[24,i], P. De Simone[28], F. De Vellis[19], J.A. de Vries[82], F. Debernardis[24], D. Decamp[10], S. Dekkers[1], L. Del Buono[16], B. Delaney[65], H.-P. Dembinski[19], J. Deng[8], V. Denysenko[51], O. Deschamps[11], F. Dettori[32,l], B. Dey[79], P. Di Nezza[28], I. Diachkov[44], S. Didenko[44], S. Ding[69], Y. Ding[50], L. Dittmann[22], V. Dobishuk[53], A. D. Docheva[60], A. Doheny[57], C. Dong[4,d], A.M. Donohoe[23], F. Dordei[32], A.C. dos Reis[2], A. D. Dowling[69], L. Dreyfus[13], W. Duan[73], P. Duda[83], L. Dufour[49], V. Duk[34], P. Durante[49], M. M. Duras[83], J.M. Durham[68], O. D. Durmus[79], A. Dziurda[41], A. Dzyuba[44], S. Easo[58], E. Eckstein[18], U. Egede[1], A. Egorychev[44], V. Egorychev[44], S. Eisenhardt[59], E. Ejopu[63], L. Eklund[85], M. Elashri[66], J. Ellbracht[19], S. Ely[62], A. Ene[43], J. Eschle[69], S. Esen[22], T. Evans[38], F. Fabiano[32], S. Faghih[66], L.N. Falcao[2], B. Fang[7], R. Fantechi[35], L. Fantini[34,s], M. Faria[50], K. Farmer[59], D. Fazzini[31,p], L. Felkowski[83], M. Feng[5,7], M. Feo[19], A. Fernandez Casani[48], M. Fernandez Gomez[47], A.D. Fernez[67], F. Ferrari[25,k], F. Ferreira Rodrigues[3], M. Ferrillo[51], M. Ferro-Luzzi[49], S. Filippov[44], R.A. Fini[24], M. Fiorini[26,m], M. Firlej[40], K.L. Fischer[64], D.S. Fitzgerald[87], C. Fitzpatrick[63], T. Fiutowski[40], F. Fleuret[15], A. Fomin[52], M. Fontana[25], L. F. Foreman[63], R. Forty[49], D. Foulds-Holt[59], V. Franco Lima[3], M. Franco Sevilla[67], M. Frank[49], E. Franzoso[26,m], G. Frau[63], C. Frei[49], D.A. Friday[63,49], J. Fu[7], Q. Führing[19,g,56], T. Fulghesu[13], G. Galati[24], M.D. Galati[38], A. Gallas Torreira[47], D. Galli[25,k], S. Gambetta[59], M. Gandelman[3], P. Gandini[30], B. Ganie[63], H. Gao[7], R. Gao[64], T.Q. Gao[56], Y. Gao[8], Y. Gao[6], Y. Gao[8], L.M. Garcia Martin[50], P. Garcia Moreno[45], J. García Pardiñas[65], P. Gardner[67], K. G. Garg[8], L. Garrido[45], C. Gaspar[49], A. Gavrikov[33], L.L. Gerken[19], E. Gersabeck[20], M. Gersabeck[20], T. Gershon[57], S. Ghizzo[29,n], Z. Ghorbanimoghaddam[55], L. Giambastiani[33,r], F. I. Giasemis[16,f], V. Gibson[56], H.K. Giemza[42], A.L. Gilman[64], M. Giovannetti[28], A. Gioventù[45], L. Girardey[63,58], M.A. Giza[41], F.C. Glaser[14,22], V.V. Gligorov[16], C. Göbel[70], L. Golinka-Bezshyyko[86], E. Golobardes[46], D. Golubkov[44], A. Golutvin[62,49], S. Gomez Fernandez[45], W. Gomulka[40], I. Gonçales Vaz[49], F. Goncalves Abrantes[64], M. Goncerz[41], G. Gong[4,d], J. A. Gooding[19], I.V. Gorelov[44], C. Gotti[31], E. Govorkova[65], J.P. Grabowski[18], L.A. Granado Cardoso[49], E. Graugés[45], E. Graverini[50,u], L. Grazette[57], G. Graziani[27], A. T. Grecu[43], L.M. Greeven[38], N.A. Grieser[66], L. Grillo[60], S. Gromov[44], C. Gu[15], M. Guarise[26], L. Guerry[11], V. Guliaeva[44], P. A. Günther[22], A.-K. Guseinov[50], E. Gushchin[44], Y. Guz[6,49], T. Gys[49], K. Habermann[18], T. Hadavizadeh[1], C. Hadjivasiliou[67], G. Haefeli[50], C. Haen[49], S. Haken[56], G. Hallett[57], P.M. Hamilton[67], J. Hammerich[61], Q. Han[33], X. Han[22,49], S. Hansmann-Menzemer[22], L. Hao[7], N. Harnew[64], T. H. Harris[1], M. Hartmann[14], S. Hashmi[40], J. He[7,e], A. Hedes[63], F. Hemmer[49], C. Henderson[66], R. Henderson[14], R.D.L. Henderson[1], A.M. Hennequin[49], K. Hennessy[61], L. Henry[50], J. Herd[62], P. Herrero Gascon[22], J. Heuel[17], A. Hicheur[3], G. Hijano Mendizabal[51], J. Horswill[63], R. Hou[8], Y. Hou[11], D. C. Houston[60], N. Howarth[61], J. Hu[73], W. Hu[7], X. Hu[4,d], W. Hulsbergen[38], R.J. Hunter[57], M. Hushchyn[44], D. Hutchcroft[61], M. Idzik[40], D. Ilin[44], P. Ilten[66], A. Iniukhin[44], A. Iohner[10], A. Ishteev[44], K. Ivshin[44], H. Jage[17], S.J. Jaimes Elles[77,48,49], S. Jakobsen[49], E. Jans[38], B.K. Jashal[48], A. Jawahery[67], C. Jayaweera[54], V. Jevtic[19], Z. Jia[16], E. Jiang[67], X. Jiang[5,7], Y. Jiang[7], Y. J.

Jiang[6], E. Jimenez Moya[9], N. Jindal[88], M. John[64], A. John Rubesh Rajan[23], D. Johnson[54], C.R. Jones[56], S. Joshi[42], B. Jost[49], J. Juan Castella[56], N. Jurik[49], I. Juszczak[41], D. Kaminaris[50], S. Kandybei[52], M. Kane[59], Y. Kang[4,d], C. Kar[11], M. Karacson[49], A. Kauniskangas[50], J.W. Kautz[66], M.K. Kazanecki[41], F. Keizer[49], M. Kenzie[56], T. Ketel[38], B. Khanji[69], A. Kharisova[44], S. Kholodenko[62,49], G. Khreich[14], T. Kirn[17], V.S. Kirsebom[31,p], O. Kitouni[65], S. Klaver[39], N. Kleijne[35,t], D. K. Klekots[86], K. Klimaszewski[42], M.R. Kmiec[42], S. Koliiev[53], L. Kolk[19], A. Konoplyannikov[6], P. Kopciewicz[49], P. Koppenburg[38], A. Korchin[52], M. Korolev[44], I. Kostiuk[38], O. Kot[53], S. Kotriakhova, E. Kowalczyk[67], A. Kozachuk[44], P. Kravchenko[44], L. Kravchuk[44], O. Kravcov[80], M. Kreps[57], P. Krokovny[44], W. Krupa[69], W. Krzemien[42], O. Kshyvanskyi[53], S. Kubis[83], M. Kucharczyk[41], V. Kudryavtsev[44], E. Kulikova[44], A. Kupsc[85], V. Kushnir[52], B. Kutsenko[13], J. Kvapil[68], I. Kyryllin[52], D. Lacarrere[49], P. Laguarta Gonzalez[45], A. Lai[32], A. Lampis[32], D. Lancierini[62], C. Landesa Gomez[47], J.J. Lane[1], G. Lanfranchi[28], C. Langenbruch[22], J. Langer[19], O. Lantwin[44], T. Latham[57], F. Lazzari[35,u,49], C. Lazzeroni[54], R. Le Gac[13], H. Lee[61], R. Lefèvre[11], A. Leflat[44], S. Legotin[44], M. Lehuraux[57], E. Lemos Cid[49], O. Leroy[13], T. Lesiak[41], E. D. Lesser[49], B. Leverington[22], A. Li[4,d], C. Li[4], C. Li[13], H. Li[73], J. Li[8], K. Li[76], L. Li[63], M. Li[8], P. Li[7], P.-R. Li[74], Q. Li[5,7], T. Li[72], T. Li[73], Y. Li[8], Y. Li[5], Y. Li[4], Z. Lian[4,d], Q. Liang[8], X. Liang[69], Z. Liang[32], S. Libralon[48], A. L. Lightbody[12], C. Lin[7], T. Lin[58], R. Lindner[49], H. Linton[62], R. Litvinov[32], D. Liu[8], F. L. Liu[1], G. Liu[73], K. Liu[74], S. Liu[5,7], W. Liu[8], Y. Liu[59], Y. Liu[74], Y. L. Liu[62], G. Loachamin Ordonez[70], A. Lobo Salvia[45], A. Loi[32], T. Long[56], J.H. Lopes[3], A. Lopez Huertas[45], C. Lopez Iribarnegaray[47], S. López Soliño[47], Q. Lu[15], C. Lucarelli[49], D. Lucchesi[33,r], M. Lucio Martinez[48], Y. Luo[6], A. Lupato[33,j], E. Luppi[26,m], K. Lynch[23], X.-R. Lyu[7], G. M. Ma[4,d], S. Maccolini[19], F. Machefert[14], F. Maciuc[43], B. Mack[69], I. Mackay[64], L. M. Mackey[69], L.R. Madhan Mohan[56], M. J. Madurai[54], D. Magdalinski[38], D. Maisuzenko[44], J.J. Malczewski[41], S. Malde[64], L. Malentacca[49], A. Malinin[44], T. Maltsev[44], G. Manca[32,l], G. Mancinelli[13], C. Mancuso[14], R. Manera Escalero[45], F. M. Manganella[37], D. Manuzzi[25], D. Marangotto[30,o], J.F. Marchand[10], R. Marchevski[50], U. Marconi[25], E. Mariani[16], S. Mariani[49], C. Marin Benito[45], J. Marks[22], A.M. Marshall[55], L. Martel[64], G. Martelli[34], G. Martellotti[36], L. Martinazzoli[49], M. Martinelli[31,p], D. Martinez Gomez[81], D. Martinez Santos[84], F. Martinez Vidal[48], A. Martorell i Granollers[46], A. Massafferri[2], R. Matev[49], A. Mathad[49], V. Matiunin[44], C. Matteuzzi[69], K.R. Mattioli[15], A. Mauri[62], E. Maurice[15], J. Mauricio[45], P. Mayencourt[50], J. Mazorra de Cos[48], M. Mazurek[42], M. McCann[62], T.H. McGrath[63], N.T. McHugh[60], A. McNab[63], R. McNulty[23], B. Meadows[66], G. Meier[19], D. Melnychuk[42], D. Mendoza Granada[16], P. Menendez Valdes Perez[47], F. M. Meng[4,d], M. Merk[38,82], A. Merli[50,30], L. Meyer Garcia[67], D. Miao[5,7], H. Miao[7], M. Mikhasenko[78], D.A. Milanes[77,z], A. Minotti[31,p], E. Minucci[28], T. Miralles[11], B. Mitreska[19], D.S. Mitzel[19], A. Modak[58], L. Moeser[19], R.D. Moise[17], E. F. Molina Cardenas[87], T. Mombächer[49], M. Monk[57,1], S. Monteil[11], A. Morcillo Gomez[47], G. Morello[28], M.J. Morello[35,t], M.P. Morgenthaler[22], A. Moro[31,p], J. Moron[40], W. Morren[38], A.B. Morris[49], A.G. Morris[13], R. Mountain[69], H. Mu[4,d], Z. M. Mu[6], E. Muhammad[57], F. Muheim[59], M. Mulder[81], K. Müller[51], F. Muñoz-Rojas[9], R. Murta[62], V. Mytrochenko[52], P. Naik[61], T. Nakada[50], R. Nandakumar[58], T. Nanut[49], I. Nasteva[3], M. Needham[59], E. Nekrasova[44], N. Neri[30,o], S. Neubert[18],

N. Neufeld[49], P. Neustroev[44], J. Nicolini[49], D. Nicotra[82], E.M. Niel[15], N. Nikitin[44], L. Nisi[19], Q. Niu[74], P. Nogarolli[3], P. Nogga[18], C. Normand[55], J. Novoa Fernandez[47], G. Nowak[66], C. Nunez[87], H. N. Nur[60], A. Oblakowska-Mucha[40], V. Obraztsov[44], T. Oeser[17], A. Okhotnikov[44], O. Okhrimenko[53], R. Oldeman[32,l], F. Oliva[59,49], E. Olivart Pino[45], M. Olocco[19], C.J.G. Onderwater[82], R.H. O'Neil[49], J.S. Ordonez Soto[11], D. Osthues[19], J.M. Otalora Goicochea[3], P. Owen[51], A. Oyanguren[48], O. Ozcelik[49], F. Paciolla[35,x], A. Padee[42], K.O. Padeken[18], B. Pagare[47], T. Pajero[49], A. Palano[24], M. Palutan[28], C. Pan[75], X. Pan[4,d], S. Panebianco[12], G. Panshin[5], L. Paolucci[63], A. Papanestis[58], M. Pappagallo[24,i], L.L. Pappalardo[26], C. Pappenheimer[66], C. Parkes[63], D. Parmar[78], B. Passalacqua[26,m], G. Passaleva[27], D. Passaro[35,t,49], A. Pastore[24], M. Patel[62], J. Patoc[64], C. Patrignani[25,k], A. Paul[69], C.J. Pawley[82], A. Pellegrino[38], J. Peng[5,7], X. Peng[74], M. Pepe Altarelli[28], S. Perazzini[25], D. Pereima[44], H. Pereira Da Costa[68], M. Pereira Martinez[47], A. Pereiro Castro[47], C. Perez[46], P. Perret[11], A. Perrevoort[81], A. Perro[49,13], M.J. Peters[66], K. Petridis[55], A. Petrolini[29,n], S. Pezzulo[29,n], J. P. Pfaller[66], H. Pham[69], L. Pica[35,t], M. Piccini[34], L. Piccolo[32], B. Pietrzyk[10], G. Pietrzyk[14], R. N. Pilato[61], D. Pinci[36], F. Pisani[49], M. Pizzichemi[31,p,49], V. M. Placinta[43], M. Plo Casasus[47], T. Poeschl[49], F. Polci[16], M. Poli Lener[28], A. Poluektov[13], N. Polukhina[44], I. Polyakov[63], E. Polycarpo[3], S. Ponce[49], D. Popov[7,49], S. Poslavskii[44], K. Prasanth[59], C. Prouve[84], D. Provenzano[32,l,49], V. Pugatch[53], G. Punzi[35,u], J.R. Pybus[68], S. Qasim[51], Q. Q. Qian[6], W. Qian[7], N. Qin[4,d], S. Qu[4,d], R. Quagliani[49], R.I. Rabadan Trejo[57], R. Racz[80], J.H. Rademacker[55], M. Rama[35], M. Ramírez García[87], V. Ramos De Oliveira[70], M. Ramos Pernas[57], M.S. Rangel[3], F. Ratnikov[44], G. Raven[39], M. Rebollo De Miguel[48], F. Redi[30,j], J. Reich[55], F. Reiss[20], Z. Ren[7], P.K. Resmi[64], M. Ribalda Galvez[45], R. Ribatti[50], G. Ricart[15,12], D. Riccardi[35,t], S. Ricciardi[58], K. Richardson[65], M. Richardson-Slipper[56], K. Rinnert[61], P. Robbe[14,49], G. Robertson[60], E. Rodrigues[61], A. Rodriguez Alvarez[45], E. Rodriguez Fernandez[47], J.A. Rodriguez Lopez[77], E. Rodriguez Rodriguez[49], J. Roensch[19], A. Rogachev[44], A. Rogovskiy[58], D.L. Rolf[19], P. Roloff[49], V. Romanovskiy[66], A. Romero Vidal[47], G. Romolini[26,49], F. Ronchetti[50], T. Rong[6], M. Rotondo[28], S. R. Roy[22], M.S. Rudolph[69], M. Ruiz Diaz[22], R.A. Ruiz Fernandez[47], J. Ruiz Vidal[82], J. J. Saavedra-Arias[9], J.J. Saborido Silva[47], S. E. R. Sacha Emile R.[49], N. Sagidova[44], D. Sahoo[79], N. Sahoo[54], B. Saitta[32,l], M. Salomoni[31,49,p], I. Sanderswood[48], R. Santacesaria[36], C. Santamarina Rios[47], M. Santimaria[28], L. Santoro [2], E. Santovetti[37], A. Saputi, D. Saranin[44], A. Sarnatskiy[81], G. Sarpis[49], M. Sarpis[80], C. Satriano[36,v], A. Satta[37], M. Saur[74], D. Savrina[44], H. Sazak[17], F. Sborzacchi[49,28], A. Scarabotto[19], S. Schael[17], S. Scherl[61], M. Schiller[22], H. Schindler[49], M. Schmelling[21], B. Schmidt[49], N. Schmidt[68], S. Schmitt[17], H. Schmitz[18], O. Schneider[50], A. Schopper[62], N. Schulte[19], M.H. Schune[14], G. Schwering[17], B. Sciascia[28], A. Sciuccati[49], I. Segal[78], S. Sellam[47], A. Semennikov[44], T. Senger[51], M. Senghi Soares[39], A. Sergi[29,n,49], N. Serra[51], L. Sestini[27], A. Seuthe[19], B. Sevilla Sanjuan[46], Y. Shang[6], D.M. Shangase[87], M. Shapkin[44], R. S. Sharma[69], I. Shchemerov[44], L. Shchutska[50], T. Shears[61], L. Shekhtman[44], Z. Shen[38], S. Sheng[5,7], V. Shevchenko[44], B. Shi[7], Q. Shi[7], W. S. Shi[73], Y. Shimizu[14], E. Shmanin[25], R. Shorkin[44], J.D. Shupperd[69], R. Silva Coutinho[69], G. Simi[33,r], S. Simone[24,i], M. Singha[79], N. Skidmore[57], T. Skwarnicki[69], M.W. Slater[54], E. Smith[65], K. Smith[68], M. Smith[62], L. Soares Lavra[59], M.D. Sokoloff[66], F.J.P. Soler[60], A. Solomin[55], A. Solovev[44], K.

Solovieva[20], N. S. Sommerfeld[18], R. Song[1], Y. Song[50], Y. Song[4,d], Y. S. Song[6], F.L. Souza De Almeida[69], B. Souza De Paula[3], K.M. Sowa[40], E. Spadaro Norella[29,n], E. Spedicato[25], J.G. Speer[19], P. Spradlin[60], V. Sriskaran[49], F. Stagni[49], M. Stahl[78], S. Stahl[49], S. Stanislaus[64], M. Stefaniak[88], E.N. Stein[49], O. Steinkamp[51], H. Stevens[19], D. Strekalina[44], Y. Su[7], F. Suljik[64], J. Sun[32], J. Sun[63], L. Sun[75], D. Sundfeld[2], W. Sutcliffe[51], V. Svintozelskyi[48], K. Swientek[40], F. Swystun[56], A. Szabelski[42], T. Szumlak[40], Y. Tan[4,d], Y. Tang[75], Y. T. Tang[7], M.D. Tat[22], J. A. Teijeiro Jimenez[47], A. Terentev[44], F. Terzuoli[35,x], F. Teubert[49], E. Thomas[49], D.J.D. Thompson[54], A. R. Thomson-Strong[59], H. Tilquin[62], V. Tisserand[11], S. T'Jampens[10], M. Tobin[5,49], T. T. Todorov[20], L. Tomassetti[26,m], G. Tonani[30], X. Tong[6], T. Tork[30], D. Torres Machado[2], L. Toscano[19], D.Y. Tou[4,d], C. Trippl[46], G. Tuci[22], N. Tuning[38], L.H. Uecker[22], A. Ukleja[40], D.J. Unverzagt[22], A. Upadhyay[49], B. Urbach[59], A. Usachov[39], A. Ustyuzhanin[44], U. Uwer[22], V. Vagnoni[25], V. Valcarce Cadenas[47], G. Valenti[25], N. Valls Canudas[49], J. van Eldik[49], H. Van Hecke[68], E. van Herwijnen[62], C.B. Van Hulse[47,aa], R. Van Laak[50], M. van Veghel[38], G. Vasquez[51], R. Vazquez Gomez[45], P. Vazquez Regueiro[47], C. Vázquez Sierra[84], S. Vecchi[26], J. Velilla Serna[48], J.J. Velthuis[55], M. Veltri[27,y], A. Venkateswaran[50], M. Verdoglia[32], M. Vesterinen[57], W. Vetens[69], D. Vico Benet[64], P. Vidrier Villalba[45], M. Vieites Diaz[47,49], X. Vilasis-Cardona[46], E. Vilella Figueras[61], A. Villa[25], P. Vincent[16], B. Vivacqua[3], F.C. Volle[54], D. vom Bruch[13], N. Voropaev[44], K. Vos[82], C. Vrahas[59], J. Wagner[19], J. Walsh[35], E.J. Walton[1,57], G. Wan[6], A. Wang[7], B. Wang[5], C. Wang[22], G. Wang[8], H. Wang[74], J. Wang[6], J. Wang[5], J. Wang[4,d], J. Wang[75], M. Wang[49], N. W. Wang[7], R. Wang[55], X. Wang[8], X. Wang[73], X. W. Wang[62], Y. Wang[76], Y. Wang[6], Y. H. Wang[74], Z. Wang[14], Z. Wang[4,d], Z. Wang[30], J.A. Ward[57], M. Waterlaat[49], N.K. Watson[54], D. Websdale[62], Y. Wei[6], J. Wendel[84], B.D.C. Westhenry[55], C. White[56], M. Whitehead[60], E. Whiter[54], A.R. Wiederhold[63], D. Wiedner[19], M. A. Wiegertjes[38], C. Wild[64], G. Wilkinson[64,49], M.K. Wilkinson[66], M. Williams[65], M. J. Williams[49], M.R.J. Williams[59], R. Williams[56], S. Williams[55], Z. Williams[55], F.F. Wilson[58], M. Winn[12], W. Wislicki[42], M. Witek[41], L. Witola[19], T. Wolf[22], E. Wood[56], G. Wormser[14], S.A. Wotton[56], H. Wu[69], J. Wu[8], X. Wu[75], Y. Wu[6,56], Z. Wu[7], K. Wyllie[49], S. Xian[73], Z. Xiang[5], Y. Xie[8], T. X. Xing[30], A. Xu[35,t], L. Xu[4,d], L. Xu[4,d], M. Xu[49], Z. Xu[49], Z. Xu[7], Z. Xu[5], K. Yang[62], X. Yang[6], Y. Yang[15], Z. Yang[6], V. Yeroshenko[14], H. Yeung[63], H. Yin[8], X. Yin[7], C. Y. Yu[6], J. Yu[72], X. Yuan[5], Y Yuan[5,7], E. Zaffaroni[50], J. A. Zamora Saa[71], M. Zavertyaev[21], M. Zdybal[41], F. Zenesini[25], C. Zeng[5,7], M. Zeng[4,d], C. Zhang[6], D. Zhang[8], J. Zhang[7], L. Zhang[4,d], R. Zhang[8], S. Zhang[72], S. Zhang[64], Y. Zhang[6], Y. Z. Zhang[4,d], Z. Zhang[4,d], Y. Zhao[22], A. Zhelezov[22], S. Z. Zheng[6], X. Z. Zheng[4,d], Y. Zheng[7], T. Zhou[6], X. Zhou[8], Y. Zhou[7], V. Zhovkovska[57], L. Z. Zhu[7], X. Zhu[4,d], X. Zhu[8], Y. Zhu[17], V. Zhukov[17], J. Zhuo[48], Q. Zou[5,7], D. Zuliani[33,r], G. Zunica[28].

[1] *School of Physics and Astronomy, Monash University, Melbourne, Australia*
[2] *Centro Brasileiro de Pesquisas Físicas (CBPF), Rio de Janeiro, Brazil*
[3] *Universidade Federal do Rio de Janeiro (UFRJ), Rio de Janeiro, Brazil*
[4] *Department of Engineering Physics, Tsinghua University, Beijing, China*
[5] *Institute Of High Energy Physics (IHEP), Beijing, China*
[6] *School of Physics State Key Laboratory of Nuclear Physics and Technology, Peking University, Beijing, China*
[7] *University of Chinese Academy of Sciences, Beijing, China*

[8] *Institute of Particle Physics, Central China Normal University, Wuhan, Hubei, China*
[9] *Consejo Nacional de Rectores (CONARE), San Jose, Costa Rica*
[10] *Université Savoie Mont Blanc, CNRS, IN2P3-LAPP, Annecy, France*
[11] *Université Clermont Auvergne, CNRS/IN2P3, LPC, Clermont-Ferrand, France*
[12] *Université Paris-Saclay, Centre d'Etudes de Saclay (CEA), IRFU, Saclay, France, Gif-Sur-Yvette, France*
[13] *Aix Marseille Univ, CNRS/IN2P3, CPPM, Marseille, France*
[14] *Université Paris-Saclay, CNRS/IN2P3, IJCLab, Orsay, France*
[15] *Laboratoire Leprince-Ringuet, CNRS/IN2P3, Ecole Polytechnique, Institut Polytechnique de Paris, Palaiseau, France*
[16] *LPNHE, Sorbonne Université, Paris Diderot Sorbonne Paris Cité, CNRS/IN2P3, Paris, France*
[17] *I. Physikalisches Institut, RWTH Aachen University, Aachen, Germany*
[18] *Universität Bonn - Helmholtz-Institut für Strahlen und Kernphysik, Bonn, Germany*
[19] *Fakultät Physik, Technische Universität Dortmund, Dortmund, Germany*
[20] *Physikalisches Institut, Albert-Ludwigs-Universität Freiburg, Freiburg, Germany*
[21] *Max-Planck-Institut für Kernphysik (MPIK), Heidelberg, Germany*
[22] *Physikalisches Institut, Ruprecht-Karls-Universität Heidelberg, Heidelberg, Germany*
[23] *School of Physics, University College Dublin, Dublin, Ireland*
[24] *INFN Sezione di Bari, Bari, Italy*
[25] *INFN Sezione di Bologna, Bologna, Italy*
[26] *INFN Sezione di Ferrara, Ferrara, Italy*
[27] *INFN Sezione di Firenze, Firenze, Italy*
[28] *INFN Laboratori Nazionali di Frascati, Frascati, Italy*
[29] *INFN Sezione di Genova, Genova, Italy*
[30] *INFN Sezione di Milano, Milano, Italy*
[31] *INFN Sezione di Milano-Bicocca, Milano, Italy*
[32] *INFN Sezione di Cagliari, Monserrato, Italy*
[33] *INFN Sezione di Padova, Padova, Italy*
[34] *INFN Sezione di Perugia, Perugia, Italy*
[35] *INFN Sezione di Pisa, Pisa, Italy*
[36] *INFN Sezione di Roma La Sapienza, Roma, Italy*
[37] *INFN Sezione di Roma Tor Vergata, Roma, Italy*
[38] *Nikhef National Institute for Subatomic Physics, Amsterdam, Netherlands*
[39] *Nikhef National Institute for Subatomic Physics and VU University Amsterdam, Amsterdam, Netherlands*
[40] *AGH - University of Krakow, Faculty of Physics and Applied Computer Science, Kraków, Poland*
[41] *Henryk Niewodniczanski Institute of Nuclear Physics Polish Academy of Sciences, Kraków, Poland*
[42] *National Center for Nuclear Research (NCBJ), Warsaw, Poland*
[43] *Horia Hulubei National Institute of Physics and Nuclear Engineering, Bucharest-Magurele, Romania*
[44] *Authors affiliated with an institute formerly covered by a cooperation agreement with CERN.*
[45] *ICCUB, Universitat de Barcelona, Barcelona, Spain*
[46] *La Salle, Universitat Ramon Llull, Barcelona, Spain*
[47] *Instituto Galego de Física de Altas Enerxías (IGFAE), Universidade de Santiago de Compostela, Santiago de Compostela, Spain*
[48] *Instituto de Fisica Corpuscular, Centro Mixto Universidad de Valencia - CSIC, Valencia, Spain*
[49] *European Organization for Nuclear Research (CERN), Geneva, Switzerland*
[50] *Institute of Physics, Ecole Polytechnique Fédérale de Lausanne (EPFL), Lausanne, Switzerland*
[51] *Physik-Institut, Universität Zürich, Zürich, Switzerland*
[52] *NSC Kharkiv Institute of Physics and Technology (NSC KIPT), Kharkiv, Ukraine*
[53] *Institute for Nuclear Research of the National Academy of Sciences (KINR), Kyiv, Ukraine*
[54] *School of Physics and Astronomy, University of Birmingham, Birmingham, United Kingdom*
[55] *H.H. Wills Physics Laboratory, University of Bristol, Bristol, United Kingdom*
[56] *Cavendish Laboratory, University of Cambridge, Cambridge, United Kingdom*
[57] *Department of Physics, University of Warwick, Coventry, United Kingdom*
[58] *STFC Rutherford Appleton Laboratory, Didcot, United Kingdom*
[59] *School of Physics and Astronomy, University of Edinburgh, Edinburgh, United Kingdom*

[60] School of Physics and Astronomy, University of Glasgow, Glasgow, United Kingdom
[61] Oliver Lodge Laboratory, University of Liverpool, Liverpool, United Kingdom
[62] Imperial College London, London, United Kingdom
[63] Department of Physics and Astronomy, University of Manchester, Manchester, United Kingdom
[64] Department of Physics, University of Oxford, Oxford, United Kingdom
[65] Massachusetts Institute of Technology, Cambridge, MA, United States
[66] University of Cincinnati, Cincinnati, OH, United States
[67] University of Maryland, College Park, MD, United States
[68] Los Alamos National Laboratory (LANL), Los Alamos, NM, United States
[69] Syracuse University, Syracuse, NY, United States
[70] Pontifícia Universidade Católica do Rio de Janeiro (PUC-Rio), Rio de Janeiro, Brazil, associated to [3]
[71] Universidad Andres Bello, Santiago, Chile, associated to [51]
[72] School of Physics and Electronics, Hunan University, Changsha City, China, associated to [8]
[73] Guangdong Provincial Key Laboratory of Nuclear Science, Guangdong-Hong Kong Joint Laboratory of Quantum Matter, Institute of Quantum Matter, South China Normal University, Guangzhou, China, associated to [4]
[74] Lanzhou University, Lanzhou, China, associated to [5]
[75] School of Physics and Technology, Wuhan University, Wuhan, China, associated to [4]
[76] Henan Normal University, Xinxiang, China, associated to [8]
[77] Departamento de Fisica , Universidad Nacional de Colombia, Bogota, Colombia, associated to [16]
[78] Ruhr Universitaet Bochum, Fakultaet f. Physik und Astronomie, Bochum, Germany, associated to [19]
[79] Eotvos Lorand University, Budapest, Hungary, associated to [49]
[80] Faculty of Physics, Vilnius University, Vilnius, Lithuania, associated to [20]
[81] Van Swinderen Institute, University of Groningen, Groningen, Netherlands, associated to [38]
[82] Universiteit Maastricht, Maastricht, Netherlands, associated to [38]
[83] Tadeusz Kosciuszko Cracow University of Technology, Cracow, Poland, associated to [41]
[84] Universidade da Coruña, A Coruña, Spain, associated to [46]
[85] Department of Physics and Astronomy, Uppsala University, Uppsala, Sweden, associated to [60]
[86] Taras Schevchenko University of Kyiv, Faculty of Physics, Kyiv, Ukraine, associated to [14]
[87] University of Michigan, Ann Arbor, MI, United States, associated to [69]
[88] Ohio State University, Columbus, United States, associated to [68]

[a] Universidade Estadual de Campinas (UNICAMP), Campinas, Brazil
[b] Centro Federal de Educacão Tecnológica Celso Suckow da Fonseca, Rio De Janeiro, Brazil
[c] Department of Physics and Astronomy, University of Victoria, Victoria, Canada
[d] Center for High Energy Physics, Tsinghua University, Beijing, China
[e] Hangzhou Institute for Advanced Study, UCAS, Hangzhou, China
[f] LIP6, Sorbonne Université, Paris, France
[g] Lamarr Institute for Machine Learning and Artificial Intelligence, Dortmund, Germany
[h] Universidad Nacional Autónoma de Honduras, Tegucigalpa, Honduras
[i] Università di Bari, Bari, Italy
[j] Università di Bergamo, Bergamo, Italy
[k] Università di Bologna, Bologna, Italy
[l] Università di Cagliari, Cagliari, Italy
[m] Università di Ferrara, Ferrara, Italy
[n] Università di Genova, Genova, Italy
[o] Università degli Studi di Milano, Milano, Italy
[p] Università degli Studi di Milano-Bicocca, Milano, Italy
[q] Università di Modena e Reggio Emilia, Modena, Italy
[r] Università di Padova, Padova, Italy
[s] Università di Perugia, Perugia, Italy
[t] Scuola Normale Superiore, Pisa, Italy
[u] Università di Pisa, Pisa, Italy
[v] Università della Basilicata, Potenza, Italy
[w] Università di Roma Tor Vergata, Roma, Italy
[x] Università di Siena, Siena, Italy
[y] Università di Urbino, Urbino, Italy

[z] *Universidad de Ingeniería y Tecnología (UTEC), Lima, Peru*
[aa] *Universidad de Alcalá, Alcalá de Henares , Spain*

[†] *Deceased*